

Short Term Variability of Evolved Massive Stars with TESS

TREVOR Z. DORN-WALLENSTEIN,¹ EMILY M. LEVESQUE,¹ AND JAMES R. A. DAVENPORT^{2,*}

¹*University of Washington Astronomy Department
Physics and Astronomy Building, 3910 15th Ave NE
Seattle, WA 98105, USA*

²*University of Washington Astronomy Department
Physics and Astronomy Building, 3910 15th Ave NE
Seattle, WA 98105, USA*

(Received January 24, 2019; Revised May 15, 2019; Accepted May 15, 2019)

Submitted to ApJ

ABSTRACT

We present the first results from a study of TESS Sector 1 and 2 light curves for eight evolved massive stars in the LMC: six yellow supergiants (YSGs) and two luminous blue variables (LBVs), including S Doradus. We use an iterative prewhitening procedure to characterize the short-timescale variability in all eight stars. The periodogram of one of the YSGs, HD 269953, displays multiple strong peaks at higher frequencies than its fellows. While the field surrounding HD 269953 is quite crowded, it is the brightest star in the region, and has infrared colors indicating it is dusty. We suggest HD 269953 may be in a post-red supergiant evolutionary phase. We find a signal with a period of ~ 5 days for the LBV HD 269582. The periodogram of S Doradus shows a complicated structure, with peaks below frequencies of 1.5 cycles per day. We fit the shape of the background noise of all eight light curves, and find a red noise component in all of them. However, the power law slope of the red noise and the timescale over which coherent structures arise changes from star to star. Our results highlight the potential for studying evolved massive stars with TESS.

Keywords: stars: massive, stars: evolution, stars: oscillations, stars: rotation, stars: variables: general

1. INTRODUCTION

The environments in and around evolved massive stars are complex and unique astrophysical laboratories. Much of the information about the physics of these stars is encoded within their variability. However, due to their rarity, the behavior of massive stars in the time domain is still poorly studied by high-precision space-based instruments. Thus, the critical physical ingredients that inform our models of evolved massive stars (e.g., the distribution of rotation rates, asteroseismically determined masses and radii, short-timescale wind-driven variability and more) are still poorly constrained by observations.

On the main sequence, massive stars manifest themselves as O and B dwarfs earlier than spectral type $\sim B3$ (Habets & Heintze 1981). During and shortly after the main sequence phase (i.e., OB dwarfs and supergiants), mass loss rates are at their lowest (Puls et al. 2008; Smith 2014), and the geometries of their circumstellar media (CSM) are at their simplest (e.g., Garcia-Segura et al. 1996; Gvaramadze et al. 2018). Thus, rotational modulation from surface features (e.g., Aerts et al. 2013; Ramiaramanantsoa et al. 2018) or Co-rotating Interaction Regions (CIRs, see Mullan 1984; Cranmer & Owocki 1996) in the stellar wind can be readily observed by *CoRoT*, *Kepler*, and K2 (see Blomme et al. 2011; Buysschaert et al. 2015; Balona et al. 2015; Balona 2016; Johnston et al. 2017, and more), and has been observed in the B supergiant HD 46769 (Aerts et al. 2013).

At shorter timescales, oscillations in main sequence B (and more recently O) stars have been detected from

Corresponding author: Trevor Z. Dorn-Wallenstein
tzdw@uw.edu

* DIRAC Fellow

space (e.g., Balona et al. 2011; Blomme et al. 2011; Buyschaert et al. 2015; Johnston et al. 2017) as p-modes in β Cephei pulsators, g-modes in Slowly Pulsating B-type (SPB) stars, or a combination of both (Daszyńska-Daszkiewicz et al. 2018). There are also sources of stochastic or noncoherent variability (Blomme et al. 2011) that could arise due to the sub-surface convection zone (which may interact with stellar pulsations, see Perdrang 2009), granulation, or inhomogeneities in the stellar wind. Additional variability may manifest itself at \sim hour timescales due to instabilities in the stellar wind (Krtićka & Feldmeier 2018). Finally, pulsations in massive stars OB supergiants have been studied both observationally (Saio et al. 2006; Aerts et al. 2017) and theoretically (e.g., Godart et al. 2009; Daszyńska-Daszkiewicz et al. 2013; Ostrowski & Daszyńska-Daszkiewicz 2015; Ostrowski et al. 2017).

Beyond these early phases, massive stars are poorly understood at short timescales. Conroy et al. (2018) demonstrated that these stars display a rich variety of variability on day to decade timescales. However, no massive stars evolved beyond the blue supergiant phase were observed at higher cadence by *Kepler* or K2, and only small samples of evolved stars at specific evolutionary phases were observed with targeted campaigns using *CoRoT* or the BRITE constellation. That said, these stars are fantastic targets for high cadence photometry. In red supergiants (RSGs), convective and pulsational processes can generate variability on long timescales (Wood et al. 1983), which helps RSGs launch dusty stellar winds (Yoon & Cantiello 2010, and references therein). Simulations of red supergiants (Chiavassa et al. 2011) predict large scale convective motions, turbulence, and shocks, all of which can manifest themselves coherently or stochastically (e.g., red noise detected in AAVSO light curves of RSGs by, Kiss et al. 2006, or the longer pulsations predicted by Yoon & Cantiello 2010).

Studies of photometric variability in Wolf-Rayet stars are still relatively few in number. The BRITE constellation has studied six of the brightest Wolf-Rayet stars (Moffat et al. 2018), and detected CIRs, binary interactions, and stochastic variability. However, with such a small sample size, little can be said about how the variability of Wolf-Rayets depends on fundamental stellar parameters like temperature and luminosity. Finally, stars in transitional states with lifetimes of only a few 10^4 years (e.g., Yellow Supergiants, luminous blue variables, “slash” stars, etc.) have gone completely unobserved, due to their rarity and thus their lack of concentration on the sky; any pointing by a mission with a stationary field of view (e.g., *Kepler*) isn’t likely to

include many short-lived evolutionary phases of massive stars. However, many of these evolutionary phases are still poorly understood. Many of them are associated with dusty circumstellar mediums, outbursts, and other phenomena. Their pulsational or rotational properties can be used to infer information about their interior states and evolution, including angular momentum transport, convection, surface differential rotation and more.

The Transiting Exoplanet Survey Satellite (TESS, Ricker et al. 2015) is a nearly all-sky photometry mission targeting \sim 20,000 bright stars per year at a two-minute cadence (with full-frame images for \sim 20 million stars every thirty minutes), yielding approximately 27 days of continuous photometry for stars close to the ecliptic plane, with longer light curves for stars observed by multiple spacecraft pointings. Large numbers of evolved massive stars in the Galaxy and the Magellanic Clouds are bright enough to be observed by TESS over the course of its nominal two-year mission. Here we present analysis of the first evolved massive star light curves to become available from TESS sectors 1 and 2. In §2, we discuss our sample selection using data from the *Gaia* mission. Results for each star are presented in §3. We discuss the relevance of our findings for stellar evolution theory, and the prospects of a dedicated TESS campaign to observe evolved massive stars in §4, before concluding in §5.

2. SAMPLE SELECTION AND DATA PROCESSING

We first attempted to search for evolved massive stars in our Galaxy, using the accurate astrometry published in the second data release (DR2) of the *Gaia* (Gaia Collaboration et al. 2018a). DR2 contains position and brightness measurements in the broad *Gaia* passband G for 1.7 billion stars, of which 1.4 billion have photometry in the blue and red bandpasses G_{BP} and G_{RP} , and 1.3 billion have parallax ϖ and proper motion μ measurements. We acquired the TESS Sectors 1 and 2 target lists¹, uploaded them to the ESA *Gaia* archive², and searched for objects in *Gaia* DR2 and the TESS target lists that were separated by less than $1''$.

In theory, *Gaia* parallaxes are easily convertible to distances via

$$\frac{d}{\text{pc}} = \frac{\text{arcsec}}{\varpi} \quad (1)$$

¹ Target lists obtainable at <https://tess.mit.edu/observations/sector-1/> and <https://tess.mit.edu/observations/sector-2/> respectively

² <https://gea.esac.esa.int/archive/>

which would allow for a direct measurement of luminosity, and then used to select massive stars. However, converting from parallax to distance is a nontrivial task in practice. Systematics — e.g., parallax and proper motion zero-point offsets measured from distant QSOs — exist in the data (Lindgren et al. 2018), and many objects have high fractional errors (σ_{ϖ}/ϖ) or negative measured parallax. In a Bayesian framework these measurements are all useful, and Bailer-Jones et al. (2018) inferred distances for the majority of stars in *Gaia* DR2 accounting for these effects, using a prior based on the spatial distribution of stars in the galaxy. For stars in the TESS–*Gaia* cross-match, we calculated the absolute G magnitude:

$$M_G = G - 5 \log_{10} r_{est} + 5 - A_G \quad (2)$$

using the estimated distance r_{est} from Bailer-Jones et al. (2018), and the published estimate of the extinction A_G . We also estimated the reddening as

$$E(G_{BP} - G_{RP}) = \frac{A_G}{A_G/A_V} \left(\frac{A_{BP}}{A_V} - \frac{A_{RP}}{A_V} \right) \quad (3)$$

using the estimated extinction A_G , and coefficients from Malhan et al. (2018). We make the cross-matched data, as well as the estimated M_G and $G_{BP} - G_{RP}$ publicly available online.³ For stars without an estimated A_G , we also estimate a lower limit to the absolute magnitude

$$M_G \leq G - 5 \log_{10} r_{est} + 5 \quad (4)$$

and an upper limit to the intrinsic $G_{BP} - G_{RP}$ by assuming $E(G_{BP} - G_{RP}) = 0$.

Because Sectors 1 and 2 contain both the Small and Large Magellanic Clouds (MCs), the Galactic prior used by Bailer-Jones et al. (2018) is inappropriate for a subset of our sample. *Gaia* Collaboration et al. (2018b) used data from *Gaia* DR2 to select likely MC members. For these stars, we adopt distance moduli of 19.05/18.52 for the SMC/LMC respectively (Kovács 2000a,b), and assume the values of R_V from Gordon et al. (2003) and $E(B - V)$ from Massey et al. (2007) to calculate the average A_G and $E(G_{BP} - G_{RP})$ towards both MCs.

We can then construct accurate color-magnitude diagrams (CMDs), which we can use to select massive stars from targets observed by TESS. We use isochrones from the MESA Isochrones & Stellar Tracks (MIST, Dotter 2016; Choi et al. 2016) group, which adopts stellar models from the Modules for Experiments in Stellar Astrophysics (MESA, Paxton et al. 2011, 2013, 2015) code. In particular we chose isochrones with metallicity

$[Fe/H] = 0.25$ for the Galaxy, and rotation speed relative to critical of $v/v_{crit} = 0.4$ — the $[Fe/H] = 0.25$ isochrones were chosen to follow the general distribution of main sequence stars, which we wish to avoid in our sample (e.g., Davenport & Covey 2018). For the LMC (SMC) we choose the corresponding $[Fe/H] = -0.5$ (-1) isochrones. We then selected the faintest isochrone point of any age between 10^5 and $10^{10.3}$ yr in steps of 0.05 dex with initial mass $M_i \geq 8 M_\odot$ in small bins of $G_{BP} - G_{RP}$. This essentially forms a boundary in color-magnitude space that represents the faintest luminosities reached by any massive star at any point during its evolution, and no fainter massive stars are expected to be found — note that many isochrone points with $M_i < 8 M_\odot$ lie above this boundary, so our sample is not constructed to be free of contamination. We show the boundary for each metallicity isochrone set, as well as *Gaia* colors and absolute magnitudes in Figure 1. Points in blue are stars for which our estimate of M_G and $G_{BP} - G_{RP}$ include the extinction, and stars in orange are those without estimates of A_G in *Gaia* DR2. Stars in green (purple) are stars belonging to the LMC (SMC), as identified by *Gaia* Collaboration et al. (2018b). The black/green/purple lines denotes our luminosity cutoff for selecting massive stars in the Galaxy/LMC/SMC.

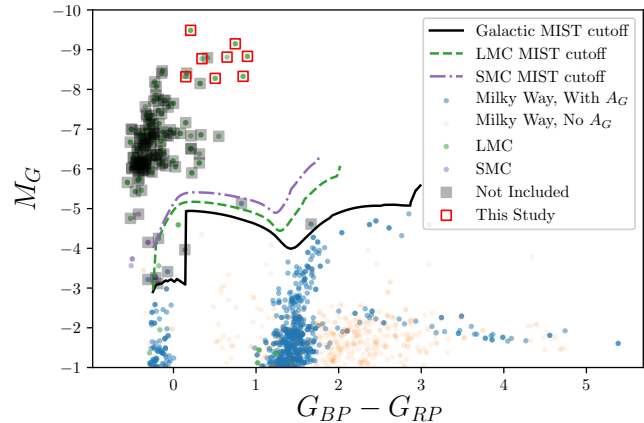


Figure 1. *Gaia* CMD for TESS Sector 1 and 2 targets. Galactic stars with an estimate of A_G are in blue, while stars without an A_G estimate are in orange; for these stars, colors are upper limits, and magnitudes are lower limits. Points in green (purple) are in the LMC (SMC). The black, green, and purple lines represent our minimum-luminosity criteria to select massive stars in the Galaxy, LMC, and SMC respectively. Stars in grey boxes are either low mass stars, or relatively unevolved O and B stars. The red boxes indicate the eight evolved massive stars we select for this study.

Of these stars, many are Galactic long period variables (LPVs), and a number are main sequence or giant OB

³ <https://github.com/tzdwi/TESS-Gaia>

Table 1. TESS two-minute cadence targets. TIC # and T magnitude are from the TIC; J magnitude is from 2MASS (Cutri et al. 2003), and 3.6, 4.5, 5.8, and 8.0 μm magnitudes are from the Spitzer SAGE LMC survey (Bonanos et al. 2009).

Common Name	Evolutionary Stage	TIC #	T	J	$J - [3.6]$	$J - [4.5]$	$J - [5.8]$	$J - [8.0]$
			[mag]	[mag]	[mag]	[mag]	[mag]	[mag]
S Dor	LBV	179305185	9.16	8.683	0.923	1.036	1.164	1.373
HD 269953	YSG	404850274	9.22	8.588	1.311	1.89	2.363	3.427
HD 269582	Ofpe/WN9 \rightarrow LBV	279957111	9.33	12.041	2.814	3.188	3.255	3.612
HD 270046	YSG	389437365	9.45	8.713	0.712	0.748	0.933	0.894
HD 270111	YSG	389565293	9.63	9.073	0.535	0.578	0.599	0.480
HD 269331	YSG	179206253	9.82	9.594	0.373	0.457	0.525	0.580
HD 269110	YSG	40404470	10.01	9.320	0.560	0.643	0.695	0.891
HD 268687	YSG	29984014	10.21	9.693	0.397	0.523	0.608	0.706

stars, as well as some Be stars, and all were observed for specific OB or Be asteroseismology programs (Pedersen et al. 2019). We also remove several targets that are not spectroscopically confirmed as massive stars, located in extremely crowded fields (with multiple bright targets located in a single 21' TESS pixel), or that are members of multiple systems (which will be studied in future work).

This leaves us with a total of eight evolved massive stars in Sectors 1 and 2 observed at two-minute cadence with TESS. All targets belong to the LMC.⁴ We list the evolutionary stage, T magnitude and ID number from the TESS Input Catalog (TIC, Stassun et al. 2018), 2MASS J magnitude (Cutri et al. 2003), and 2MASS/IRAC colors using data from Bonanos et al. (2009) in Table 1. We indicate the locations of these stars with red boxes in Figure 1. Points outlined in grey boxes are either low mass AGB LPVs or relatively unevolved O and B stars that we ignore for this study. We note that, while this CMD-based selection was redundant for selecting our sample of luminous and well-known LMC stars, it is useful for selecting Galactic stars.

2.1. Data Cleaning

The TESS team released raw light curves and full-frame images from Sectors 1 and 2 on 6 December 2018. We downloaded all light curves for stars observed at two-minute cadence from The Mikulski Archive for Space Telescopes (MAST), and selected the light curves associated with the TIC numbers of our targets. Because these light curves are processed by the first iteration

of the TESS pipeline, we err on the side of caution, assuming that the raw light curves contain numerous instrumental effects. Thus we select the PDCSAP_FLUX lightcurves, which have been corrected for some systematics. We then normalize by dividing the data by the median flux. For targets observed in both Sectors 1 and 2, we choose to median-divide each Sector individually before concatenating the light curves. While this helps to eliminate Sector-to-Sector offsets and systematics, it can also erase variations at timescales longer than ~ 1 month. We plot all of the normalized light curves, along with a rolling 128-point median in orange, in Figure 2. Finally, for HD 268687, we fit the light curve with a 7th-order polynomial, and normalize the data by the fit in order to remove the increase in flux at the beginning of the light curve that would mask otherwise interesting behavior. This effectively acts as a low-pass filter in the Fourier domain. The resulting data have pseudo-Nyquist frequencies f_{Ny} (calculated from the average time-difference between data points) between 320 and 330 day^{-1} . Due to the ~ 30 -day observing window per TESS sector, the expected width of peaks in the periodograms presented (the Rayleigh resolution, defined as the inverse of the observing baseline T) is 0.036 day^{-1} for HD 269582, HD 270111, and HD 269331, and 0.018 day^{-1} for the remaining stars.

2.2. Iterative Prewhitening

We now wish to describe the variability of each star in terms of sinusoids. For this, we apply the following prewhitening procedure for each lightcurve, as described in Blomme et al. (2011). We first subtract the mean value of the flux. We then use Astropy (Astropy Collaboration et al. 2013; The Astropy Collaboration et al. 2018) to calculate the Lomb-Scargle Periodogram (Lomb 1976; Scargle 1982) on the unsmoothed data for frequen-

⁴ As an aside: the fact that all of these stars are in the LMC emphasizes the need for TESS programs targeting Galactic evolved massive stars, where the targets are brighter and less crowded.

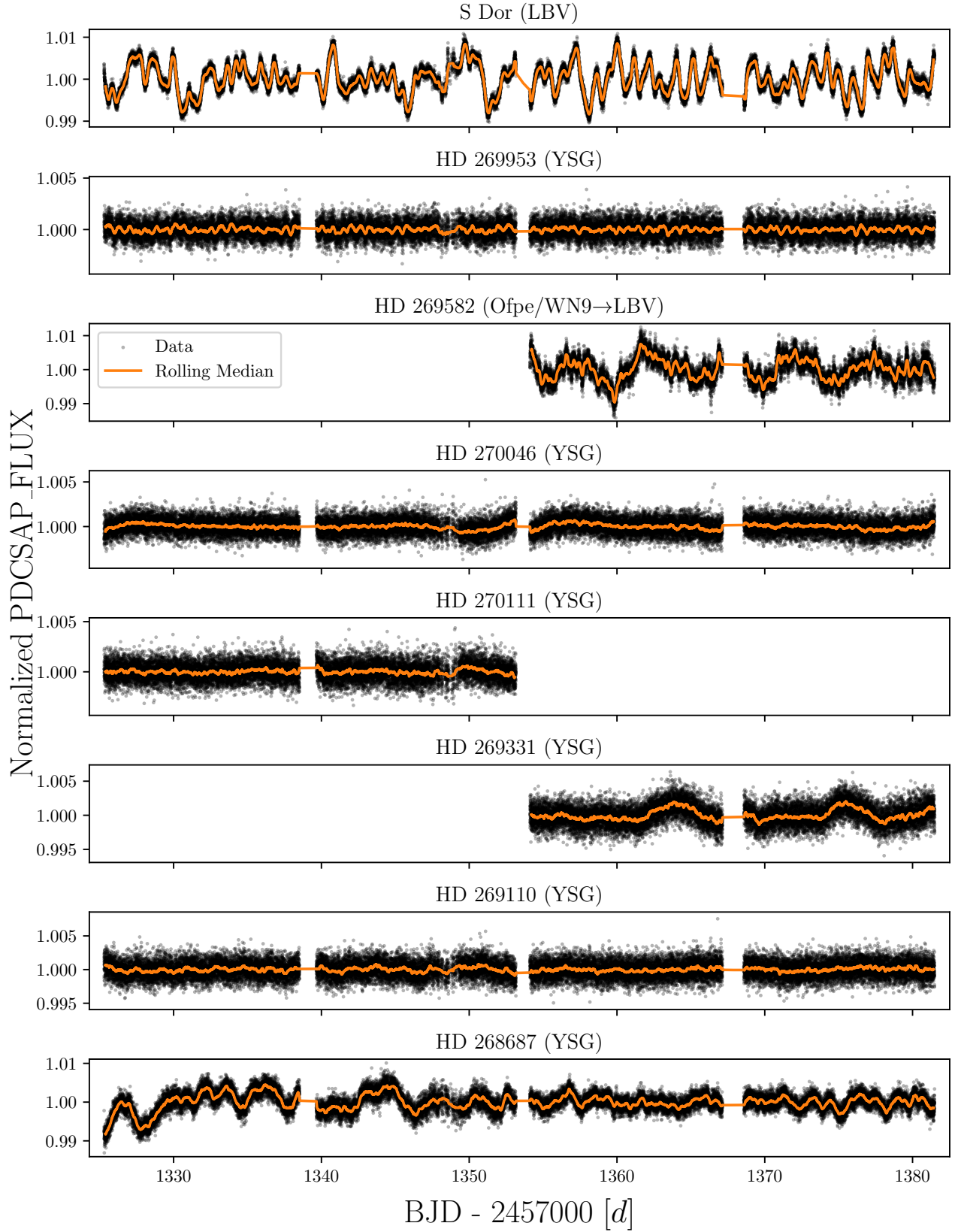


Figure 2. Normalized TESS light curves for the eight target stars. Data are in black points, and a rolling 128-point median is plotted in orange.

cies between $1/30 \text{ day}^{-1}$ and f_{Ny} , adopting the default Astropy grid-spacing heuristic of 5 times the Rayleigh resolution. The lower frequency limit is set to avoid overinterpreting low-frequency systematics that may exist between TESS sectors. Using the `psd` normalization, the resulting periodograms are in units of power.

At the j^{th} stage of prewhitening, we calculate the periodogram, and select the frequency of the peak with the highest power, f_{max} . We then use the `curve_fit` routine in SciPy Jones et al. (2001–) to fit the current prewhitened flux at each time t_i with a sin function $A_j \sin(2\pi f_j t_i + \phi_j)$, where A_j is the semi-amplitude, f_j is the frequency, and ϕ_j is the phase. A_j and ϕ_j are allowed to vary freely, and f_j is bound to the range $f_{max} \pm 1/T$. To calculate the errors on each parameter, we use the formulae given in Lucy & Sweeney (1971) and Montgomery & Odonoghue (1999):

$$\epsilon(f_j) = \sqrt{\frac{6}{N}} \frac{1}{\pi T} \frac{\sigma_j}{A_j} \quad (5)$$

$$\epsilon(A_j) = \sqrt{\frac{2}{N}} \sigma_j \quad (6)$$

$$\epsilon(\phi_j) = \sqrt{\frac{2}{N}} \frac{\sigma_j}{A_j} \quad (7)$$

$$(8)$$

where σ_j is the standard deviation of the flux at the j^{th} prewhitening stage.

We then subtract the fit from the flux and begin the next phase. As a stopping criterion, we adopt the Bayesian Information Content (BIC, Schwarz 1978)

$$BIC = -2 \ln(\mathcal{L}) + m \ln(N) \quad (9)$$

where m is the total number of terms in the fit ($\equiv 3j$), N is the number of points in the lightcurve, and \mathcal{L} is the likelihood, defined such that

$$-2 \ln(\mathcal{L}) = \sum_{i=1}^N \frac{(y_i - F(t_i, \Theta_m))^2}{\sigma_i^2} \quad (10)$$

to within a constant, where y_i are the original normalized fluxes, $F(t_i, \Theta_m)$ is the sum of all of the fit sinusoids in the current and preceding prewhitening stages evaluated at times t_i and fit parameters Θ_m , and σ_i are the normalized errors in the original light curve (Press et al. 1992, Sect. 15.1). To determine when we have reached the noise level of the light curve, we continue prewhitening until we reach a minimum in the fit's BIC.

This procedure results in a list of frequencies, amplitudes, and phases that can, in principle, describe the variability of each star. However, a number of the derived frequencies are quite similar to each other (i.e.,

the difference in frequencies is within the Rayleigh resolution). These similar and spurious frequencies can arise due to the short length of the observing baseline (Loumos & Deeming 1978). Therefore, we filter the list of frequencies by imposing a requirement that frequencies must be separated by more than $1.5/T$. In cases where such pairs of similar frequencies are found, we discard the frequency found at the later stage of prewhitening. We list N , f_{Ny} , the Rayleigh resolution $1/T$, the number of frequencies found via prewhitening, and the number of unique frequencies in Table 2. The unique frequencies, amplitudes, and phases (as well as corresponding formal errors) found for each star are listed in §A.

We note that, while this prewhitening procedure is capable of accurately describing the TESS light curves, significant frequency-dependent astrophysical and instrumental noise exists in these data, and produces spurious coherent structures that may be mistaken for periodicity. Determining the significance of a detected periodic signal under the null hypothesis of such noise is a non-trivial task. While analytic methods exist to estimate significance in the case of white or power-law noise (e.g., Baluev 2008; Vaughan 2005), significance tests in the case of a more complex noise model are inconsistent in various subfields in the literature. No suitable physical model for the astrophysical noise, represented in Equation (15), has been proposed; therefore, any estimate of the significance of the frequencies found here would be model dependent. However, we do test to determine if the value of the periodogram peaks closest to the recovered frequencies exceed a power corresponding to a false-alarm level of 1% under the null hypothesis of white noise, as described by Baluev (2008), and note the cases where frequencies discussed do not, both in text and in §A.

In the case of the red noise discussed below, Blomme et al. (2011) present a method of evaluating the significance of frequencies under noise of the form discussed here. After fitting the periodogram with Equation (15), we rescale the noise function so that the integral over the frequency range considered is equal to the variance of the flux times f_{Ny} . For each frequency, we evaluate:

$$P(z > Z) = 1 - e^{-e^{-0.93Z + \ln(0.8N)}} \quad (11)$$

which gives the probability that a stochastic noise process would result in an amplitude z that exceeds a threshold

$$Z(f) = \frac{A_j^2 N}{4\sigma_{red}^2} \quad (12)$$

where A_j is the amplitude found by prewhitening, N is the number of points in the lightcurve, and σ_{red} is

the value of the rescaled noise function at the frequency under consideration. A frequency is considered significant under red noise if $P < 0.01$. Suspiciously, all frequencies found are significant under this criterion. As we mention above, this result is likely model dependent; it is possible that many of these frequencies (if not all in some cases) are entirely attributable to the noise process. Future TESS sectors will provide insight into the low frequency regime, and allow us to conduct, for example, time-frequency analyses over a much longer baseline to determine the persistence of these frequencies. Finally, we estimate the signal-to-noise ratio (SNR) for each frequency, calculated as the ratio of the amplitude to the standard deviation of the lightcurve after prewhitening. While more straightforward, this estimate of the significance of each frequency is also flawed, as no frequency has $SNR > 2$, despite all frequencies included quantitatively improving the overall fit to the lightcurve according to the adopted BIC criterion (Equation (9)). Indeed many of these frequencies being visible by eye in the lightcurves in Figure 2. Nevertheless, we include the measured SNR in the tables in §A.

3. RESULTS

3.1. Yellow Supergiants

A $25 M_{\odot}$ solar-metallicity will begin its life as an O star; in the Geneva evolutionary tracks (Ekström et al. 2012) this star is an O6 dwarf on the zero-age main sequence. After 7 Myr, it has evolved into a B0 supergiant, at which point it crosses the HR diagram in under a Myr to become a RSG. Approximately 500 kyr later, it has evolved bluewards once more to become a Wolf-Rayet star (Massey et al. 2017). During both rightward and leftward crossings of the HR diagram, the star undergoes an incredibly brief yellow supergiant (YSG) phase. Thus, while the luminosities and effective temperatures of two given YSGs may be identical, their initial masses, ages, and interior structures may be radically different. Signatures of these differences may be imprinted in the TESS lightcurves. While it is likely that a cool YSG that has previously undergone a RSG phase will be accompanied by a dusty envelope, as the star’s effective temperature increases, the dust may be photodissociated, which is consistent with the decreasing abundance of circumstellar dust species around increasingly hot evolved massive stars in Table 1 of Waters (2010). Therefore, it is possible that variability may be the best or most unambiguous means of distinguishing between rightward- and leftward-moving YSGs. Finding leftward-moving YSGs places a valuable upper limit on the initial masses of stars that explode as RSGs before

they can become YSGs (a.k.a., “the red supergiant problem”, e.g., Smartt et al. 2009).

3.1.1. HD 269953

HD 269953 is a G0 YSG, assigned a luminosity class of 0 by Keenan & McNeil (1989), which is in agreement with its high luminosity $\log(L/L_{\odot}) = 5.437$ from Neugent et al. (2012). Coupled with its temperature $T_{eff} = 4920$ K, this implies a radius of $566 R_{\odot}$ from the Stephan-Boltzmann law. While the light curve presented in Figure 2 appears to be dominated by noise, the light curve smoothed by a 128-point rolling median appears to show coherent oscillations. We re-plot the smoothed, mean-subtracted light curve in the top panel of Figure 3. The periodogram, plotted in the lower panel of Figure 3 shows multiple strong peaks at frequencies above 1 day^{-1} . The prewhitening procedure described in §2.2 reveals the presence of 14 unique frequencies, indicated by the vertical black lines. We search for harmonics of the form f_1/f_0 that satisfy

$$nf_0 - f_1 \leq \sqrt{(n\epsilon(f_0))^2 + (\epsilon(f_1))^2} \quad (13)$$

where n is an integer greater than 1. In the light curve of HD 269953, we detect the first ($n = 2$) and second ($n = 3$) harmonics of $f = 1.3347924 \text{ day}^{-1}$, which we indicate with the vertical red lines. While we search for harmonics up to $n = 10$ for all sources, the low amplitudes and frequency resolution make it unlikely that any high harmonics found are real, and we caution against over-interpreting high harmonics that may not exist. For example, this search also revealed the ninth harmonic of $f = 0.26019548 \text{ day}^{-1}$. The corresponding peak in the periodogram does not surpass the 1% false alarm level; because of this fact, along with the null detection of any of the preceding harmonics, we deem this to be a chance coincidence.

We also searched for frequency combinations in the form $f_0 + f_1 = f_2$, such that

$$f_0 + f_1 - f_2 \leq \sqrt{(\epsilon(f_0))^2 + (\epsilon(f_1))^2 + (\epsilon(f_2))^2} \quad (14)$$

We find that the strongest peak in the periodogram at $1.59360677 \text{ day}^{-1}$ can be represented as the sum of two peaks at 0.26019548 and $1.3347924 \text{ day}^{-1}$. If variability at these frequencies is driven by pulsations, this may indicate that some of the modes are interacting with each other.

With high amounts of IR reddening, HD 269953 is the dustiest YSG in our sample, making it quite likely that it is in a post-RSG phase. Thus, a direct measurement of its mass via asteroseismology, using the multiple sets of

Table 2. Summary of light curve characteristics. .

Common Name	N	f_{Ny} [day ⁻¹]	$1/T$ [day ⁻¹]	Number of frequencies	Unique frequencies
S Dor	36296	322.8060468379108	0.0177879072510214	71	41
HD 269953	36418	323.89171072083246	0.01778794028727421	14	14
HD 269582	18226	332.52345927965945	0.036490914598590884	33	25
HD 270046	36291	322.76203971547	0.017787932748165886	14	10
HD 270111	18101	324.59880106819276	0.03586727083626439	7	6
HD 269331	18279	333.49073111685124	0.03649094333262405	10	6
HD 269110	36403	323.7577400015701	0.017787909455610686	11	7
HD 268687	36412	323.83746567083887	0.017787891882718898	64	33

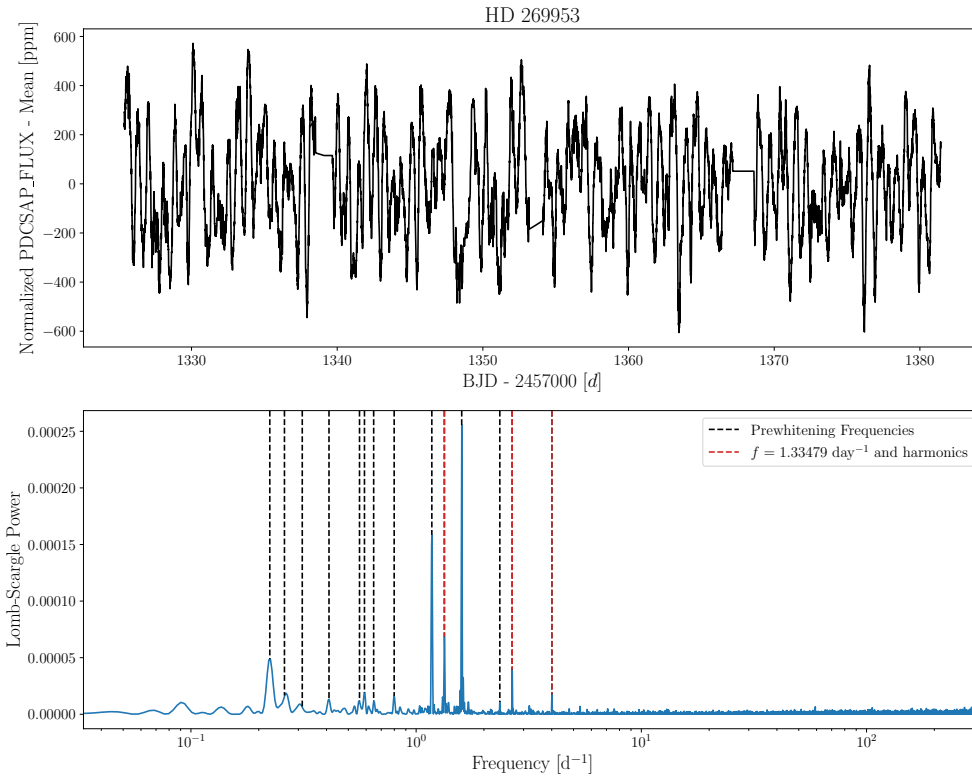


Figure 3. *Top:* Light curve for HD 269953, after smoothing with a 128-point rolling median, showing coherent variability at approximately 600 ppm. *Bottom:* Lomb-Scargle Periodogram. The black lines indicate frequencies found via prewhitening. The $f = 1.33479 \text{ day}^{-1}$ peak and its two detected harmonics are indicated with red vertical lines.

frequencies presented here would be an incredibly valuable constraint on stellar evolution. Unfortunately, it is located in the star-forming LMC cluster NGC 2085, and thus is subject to a high degree of crowding in TESS’s 21” pixels. While HD 269953 is the brightest star by far

in the field, we reserve further analysis of the light curve until more advanced tools are developed to extract light curves from crowded regions in TESS. Regardless, it is readily apparent that the periodogram of HD 269953 is different from the periodograms of the two other YSGs

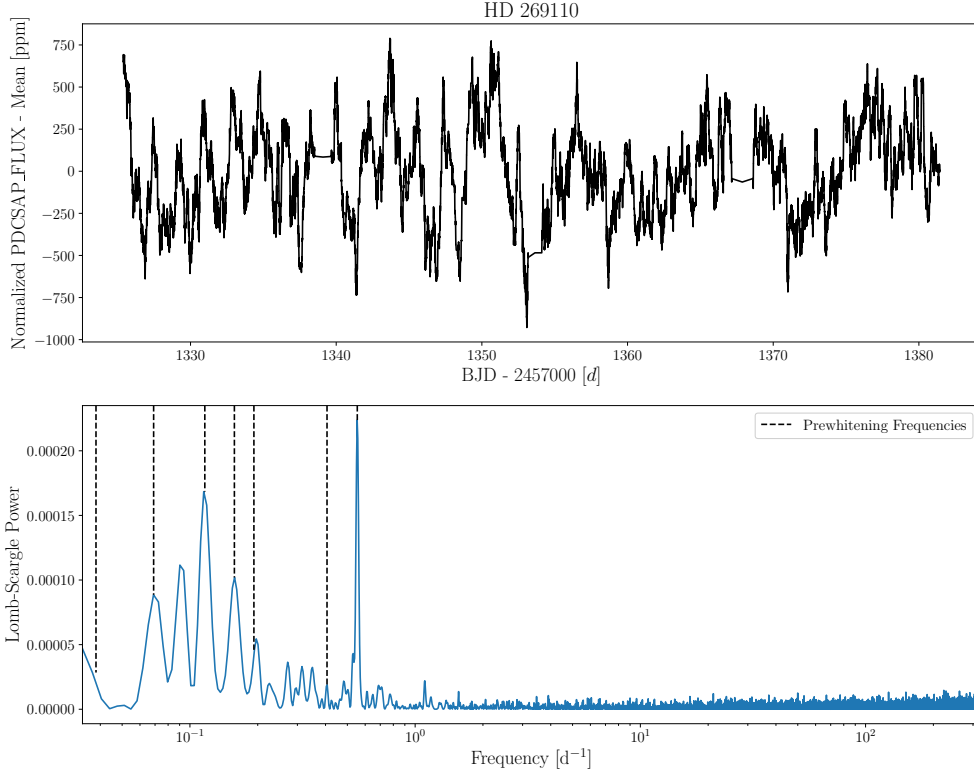


Figure 4. Similar to Figure 3, for HD 269110.

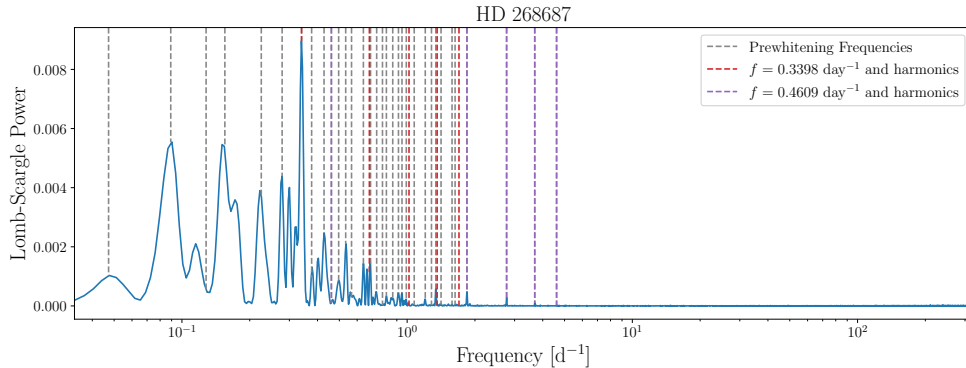


Figure 5. Similar to the bottom panel of Figure 3 for HD 268687. We indicate the strongest peak and its first four harmonics with vertical red lines; these harmonics were not detected via the procedure described in §2.2. We also find harmonics of a $\sim 0.4609 \text{ day}^{-1}$ signal, indicated in purple.

discussed below. The strongest peaks in its periodogram are located at almost an order of magnitude higher frequency, and it displays very little of the low frequency peaks seen in the periodograms of the other YSGs. Additionally, the slope of the background noise (discussed further below) is much flatter. Coupled with its appar-

ently more-evolved state, this suggests a distinct difference in variability between pre- and post-RSG yellow supergiants.

3.1.2. HD 269110 & HD 268687

HD 269110 is a lower luminosity YSG with $\log(L/L_{\odot}) = 5.251$, $T_{eff} = 5624 \text{ K}$ (Neugent et al. 2012), and thus

a radius of $445 R_{\odot}$. It has a spectral type of G0I from [Ardeberg et al. \(1972\)](#). Similar to HD 269953, the light curve presented in Figure 2 appears to be just noise, while the light curve smoothed by a 128-point rolling median shows coherent variability at approximately 750 ppm. Figure 4 shows the smoothed, mean-subtracted light curve in the top panel, and the periodogram in the bottom. Prewhitening reveals a set of 7 unique frequencies in the lightcurve. On average, these frequencies are lower than those found in the other YSGs. With physical properties and photometry consistent with all other YSGs other than HD 269953, it is not clear why might be the case; it is possible that, as the second-faintest star in the sample, we simply don't detect higher frequency signals. The strongest peak at 0.55 day^{-1} (a period of 1.81 days) has its first harmonic visible; however, it was not recovered by our prewhitening procedure. [Blomme et al. \(2011\)](#) found that the BIC was the most conservative stopping criterion in their prewhitening procedure, resulting in the fewest detected frequencies (which may also explain why we do not recover one of the low frequency peaks seen in the periodogram). Alternatively, this harmonic may not be real. Data from future TESS sectors will allow us to more firmly establish or disprove the existence of this harmonic. A group of peaks centered at $\nu_{max} = 0.115 \text{ day}^{-1}$ with an average frequency spacing $\Delta\nu = 0.032 \text{ day}^{-1}$ is also visible. Similar structures have been found in the periodograms of many pulsating stars, and asteroseismic models have yielded precise measurements of their masses and deep insight into their core structures. Comparable measurements of evolved massive stars would provide a previously inaccessible constraint on a poorly understood phase of massive stellar evolution. However, suitable models of YSG pulsations at these timescales do not yet exist.

HD 268687 is classified as a F6Ia supergiant by [Ardeberg et al. \(1972\)](#), and has a luminosity $\log(L/L_{\odot}) = 5.169$ and effective temperature $T_{eff} = 6081 \text{ K}$ from [Neugent et al. \(2012\)](#), implying a radius of $346 R_{\odot}$. The periodogram, shown in Figure 5, with prewhitening frequencies shown in grey, displays a clear peak at 0.3398 day^{-1} , corresponding to a period of 2.95 days, which is readily visible in the light curve. We indicate this frequency and its first four harmonics with vertical red lines; none of these exact harmonics are found by prewhitening, however, many of the frequencies recovered are close to the harmonics (though the latter three do not surpass the 1% false alarm level). Additionally, the series of peaks at $\sim 0.3 \text{ day}^{-1}$ appears to repeat with smaller amplitudes at a spacing of $\sim 1.2 \text{ day}^{-1}$ until $\sim 0.8 \text{ day}^{-1}$, though the exact shape of the peaks changes. The autocorrelation function calculated

from the periodogram has a series of peaks with Δf between 0.06 and 0.25 day^{-1} . A total of 33 unique frequencies are revealed by prewhitening, making its lightcurve the most complex of the YSGs studied. We do recover the third ($n = 4$), fifth, seventh, and ninth harmonics of $f = 0.46094861 \text{ day}^{-1}$ (the last of which does not surpass the 1% false alarm level), which we indicate with vertical purple lines. While the fundamental corresponds to a minimum in the periodogram, the harmonics correspond to the only peaks above $\sim 2 \text{ day}^{-1}$. Our search for combinations of frequencies yields two frequencies (0.86314365 and $1.07507415 \text{ day}^{-1}$) that mix with the dominant 0.3398 day^{-1} signal, along with 8 other combinations. Finally, a broad bump of peaks accompany the dominant peak at lower frequencies.

All told, both YSGs are in similar physical states, and both show clear peaks in their periodograms on timescales of 2-3 days, in addition to structure at higher frequencies, and a series of peaks at lower frequencies. We can rule out some possible sources of the dominant signal in both light curves. If both stars are approximately $25 M_{\odot}$ and the variability is due to binary interactions with a companion, the companion would have to be approximately $64,000 M_{\odot}$ to be in a 2.95-day Keplerian orbit outside of the stellar surface of HD 268687, and $360,000 M_{\odot}$ to be in a 1.81-day Keplerian orbit around HD 269110. We determine both scenarios to be highly implausible.

Perhaps the brightness modulations are instead due to one or more spots on the surface of the stars, causing the apparent luminosity to change as the star rotates? If the typical spot latitude were at the stellar equator, then the star would be rotating at approximately $6,000 \text{ km s}^{-1}$ for HD 268687, and $12,000 \text{ km s}^{-1}$ for HD 269110, well beyond the critical velocity for both stars. However, we cannot rule out a nearly-polar spot. This option is somewhat attractive given the change in the shape of the variability in HD 268687 with time, but would require invoking severe surface differential rotation, as well as extremely fast spot decay times to explain the change of the variability in HD 269110.

The final possibility, which is also consistent with the change in the shape of the variability, is that we are observing coherent pulsational variability in both stars, in addition to the apparent ‘‘frequency comb’’ seen in the periodogram of HD 269110. YSGs have been observed to vary with periods of many tens of days ([Arellano Ferro 1985](#)) caused by He ionization-driven radial pulsations. Perhaps we are observing a very high-order harmonic of a radial mode. Alternately, oscillations in a non-radial mode may be causing this variability. Because both stars are in the LMC, it, and most of our other tar-

gets, are in the TESS Continuous Viewing Zone (CVZ), and will be observed almost continuously for a year. If this variability is caused by p- or g-mode pulsations, some of the peaks in the periodogram may resolve into additional frequency combs characteristic of these pulsations. Another option is that the variability is caused by Rossby waves (or r-mode oscillations, Papaloizou & Pringle 1978), which appear as “hump and spike” shapes in the periodogram (Saio et al. 2018), which have been observed in main sequence F and G stars. While the fundamental mode is located at a slightly lower frequency than the rotational frequency (and hence we run into the same problems as above), higher-azimuthal-order frequencies can arise. Unfortunately the amplitude of the oscillations declines sharply at the higher orders, implying that the rotation speeds would only be a factor of a few slower, which is still physically implausible.

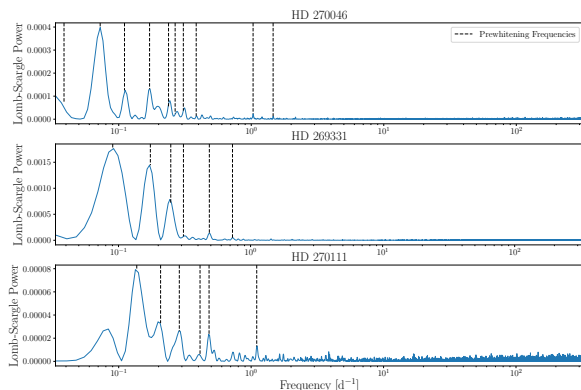


Figure 6. Similar to Figure 5 for HD 270046, HD 269331, and HD 270111.

3.1.3. HD 270046, HD 269331, & HD 270111

Two of the remaining three YSGs, HD 270046 and HD 270111, have been poorly studied thus far, and display minimal variability in these data. The 5th data release of the RAdial Velocity Experiment (RAVE, Kunzler et al. 2017) contains data for HD 270046. While the multiple optical spectra obtained by RAVE yield a wide range of atmospheric parameters (and distances inconsistent with HD 270046’s membership in the LMC), measurements of T_{eff} inferred from infrared flux are all between 6200 and 6360 K, with a mean of 6275 K. We were unable to find atmospheric parameters for HD 270111. However, with spectral types of F8Ia and G5I, and TESS magnitudes/infrared colors consistent with HD 269110 and HD 268687, it is fair to assume both stars are fairly typical yellow supergiants. The final YSG, HD 269331, has atmospheric parameters from

Neugent et al. (2012). While its temperature is consistent with the other YSGs in their sample, Ardeberg et al. (1972) assign a spectral type of A5Ia to HD 269331. Its lightcurve (Figure 2) displays two prominent bumps. However, HD 269331 was not observed by TESS in Sector 1, so we are unable to see if these bumps are repeating patterns. We present the periodograms of all three stars in Figure 6.

Prewhitening reveals the presence of 10, 6, and 6 unique frequencies in the lightcurves of HD 270046, HD 269331, and HD 270111 respectively, none of which have a normalized semi-amplitude larger than 0.0002, and no peaks surpass the 1% false alarm level. Some higher order ($n \geq 7$) harmonics of various frequencies are found in HD 270046, which we dismiss as coincidental. We also see a combination of the highest peak at $f = 0.07243 \text{ day}^{-1}$ and the lowest frequency detected at 0.03865 day^{-1} , seen at 0.11055 day^{-1} . However, it appears as if the low frequency detected by prewhitening corresponds to a peak in the periodogram that actually lies below our minimum frequency cutoff. In HD 270111, we detect the second and seventh harmonics of the strongest peak at $f = 0.136908 \text{ day}^{-1}$; the second harmonic is also the first harmonic of the small peak at $0.207207 \text{ day}^{-1}$. With such small amplitudes relative to the noise in the light curve, we refrain from discussing these patterns until higher signal to noise periodograms are obtainable with future TESS sectors.

3.1.4. Noise Properties of YSG Light Curves

In addition to the peaks in periodograms of the three YSGs discussed above, background noise exists for all six YSGs. Is this noise instrumental or astrophysical? Astrophysical red noise is seemingly ubiquitous in the light curves of hot massive stars as discussed in §1, and thus it would be unsurprising for it to manifest in these cooler stars. When plotted in log-scale, some of the periodograms in Figure 7 appear to display red noise (especially HD 268687). To model the background, we follow Blomme et al. (2011), and use `curve_fit` to fit the Lomb-Scargle periodogram with the function

$$\alpha(f) = \frac{\alpha_0}{1 + (2\pi\tau f)^\gamma} + \alpha_w \quad (15)$$

from Stanishchev et al. (2002), where f is the frequency, α_0 is the power as $f \rightarrow 0$, τ is a characteristic timescale, and α_w is an additional parameter we add in to model the white noise floor at the highest frequencies (ostensibly equal to the instrumental noise). We perform this fit after calculating the base-10 logarithm of both the Lomb-Scargle power and the fitting function to avoid artificial weighting of real peaks at high frequencies.

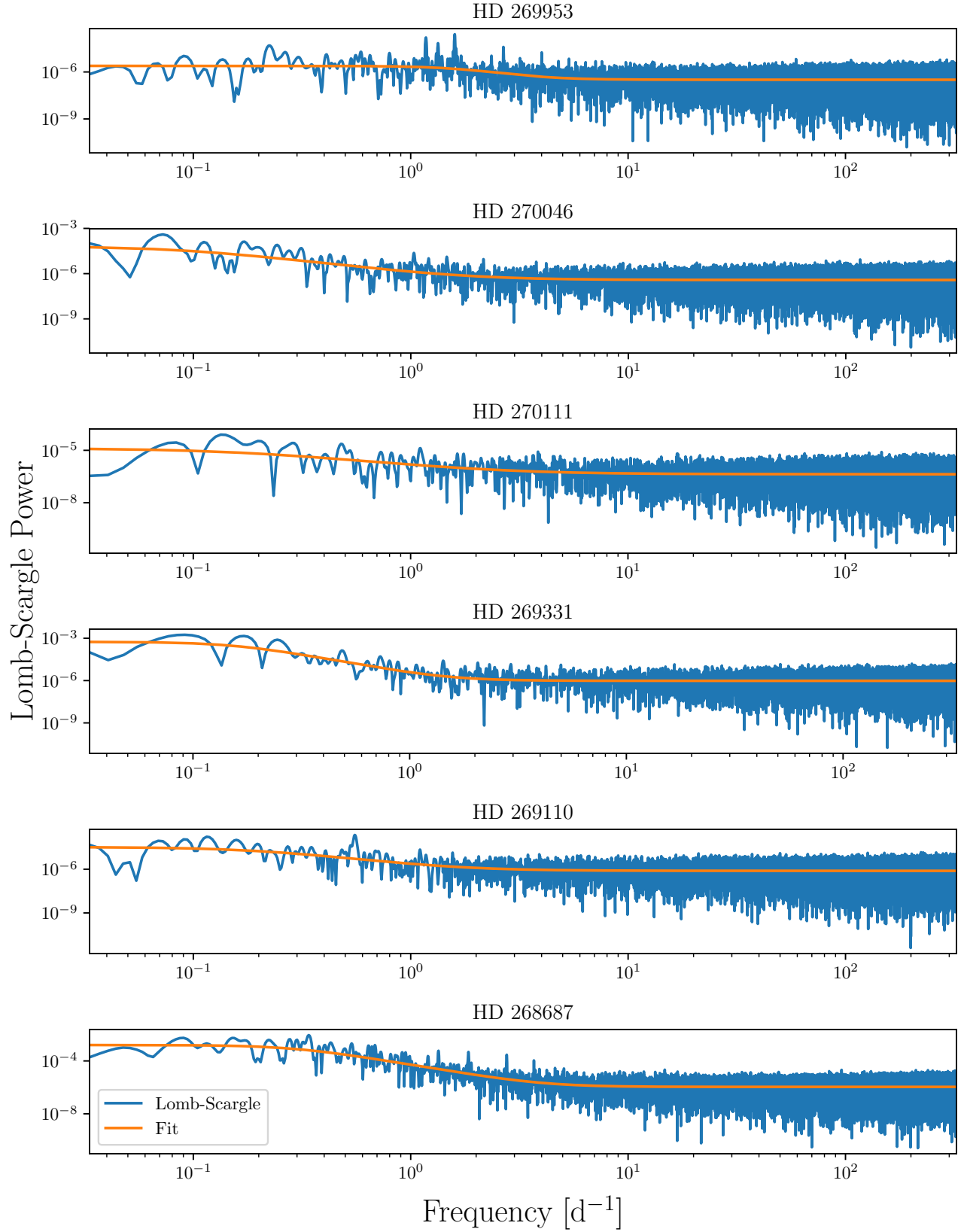


Figure 7. Lomb-Scargle periodograms calculated between $1/30 \text{ day}^{-1}$ and the pseudo-Nyquist frequency for all six YSGs. Fits using equation (15) are in orange.

The periodograms and fits for all six YSGs are shown in Figure 7. The parameter values and 1σ error estimates are compiled in Table 3, and compared to the physical properties of the stars when available in Neugent et al. (2012). It is immediately clear that the noise characteristics of all of the light curves differ, indicating that the source of the noise is likely astrophysical. HD 269953 is quantitatively different from the other YSGs in all parameters but the white noise component of the fit. Notably the red noise power-law component of the fit is only readily apparent over a narrow range of frequencies $\sim 2-4 \text{ day}^{-1}$, but the power law slope is approximately twice as steep as all YSGs but HD 268687. Combined with its status as the dustiest YSG in the sample, it is clear that this object warrants further follow-up in the short-timescale regime. Finally, both of the F supergiants have significantly higher power at the lowest frequencies (α_0) especially HD 268687. With a larger sample of YSGs, comparisons between physical quantities and noise parameters will help constrain the origin of this noise, which has not been detected until now.

3.2. Luminous Blue Variables

Arguably one of the least understood stellar evolutionary phases, luminous blue variables (LBVs) are a phenomenological class consisting of extremely luminous stars that show signs of dramatic variability. LBVs are perhaps best characterized by their giant eruptions (such as those famously associated with η Carina and P Cygni), bright enough to be mistaken as supernovae. In some cases these "impostor" events are followed by true supernovae on timescales of a few years, as in the case of SN 2009ip, which underwent two outbursts in 2009 and 2010 before potentially undergoing a terminal explosion in 2012, e.g. (Mauerhan et al. 2013; Fraser et al. 2015). However, LBVs also experience large episodic variations in their effective temperatures on timescales of months to years, known as "S Dor variations". With their bolometric luminosities remaining almost constant, these S Dor variations manifest as horizontal evolution on the Hertzsprung-Russell diagram between their hot and cool states. LBVs also exhibit ~ 0.1 mag irregular microvariability on timescales of weeks to months (Abolmasov 2011).

The evolutionary state of LBVs, their status as single or binary stars, and the physical mechanisms driving the S Dor variations are all topics of current debate (see Smith & Tombleson 2015; Humphreys et al. 2016; Aadland et al. 2018, Levesque & Lamers 2019). One possibility is that pulsations may be important for driving mass loss for S Doradus variability (Lovekin & Guzik 2014), and may therefore be observable. Indeed, a sim-

ple estimate of the dynamical/free-fall timescale for a typical LBV from Abolmasov (2011) yields

$$t_{dyn} \approx 0.6 \left(\frac{R_*}{10^{12} \text{cm}} \right)^{3/2} \left(\frac{M_*}{100 M_\odot} \right)^{-1/2} \text{ d} \quad (16)$$

and variability on this timescale is easily observable by TESS. However, LBVs tend to be surrounded by a complex and sometimes dusty CSM — indeed, both LBVs studied here have incredibly red colors in Table 1 — so these pulsations may be attenuated and modulated by this intervening material. All told, understanding the short timescale variability of LBVs can offer incredibly valuable insight into the physical state of LBVs and their immediate environments.

3.2.1. HD 269582

HD (sometimes HDE) 269582 was observed as a H-rich Ofpe/WN9 or WN10h Wolf-Rayet star as recently as the mid 1990s (Crowther & Smith 1997). However, since 2003, it has entered an outbursting LBV state, rapidly brightening in V -band as it cooled to a late-B/early-A spectral type, accompanied by drastic changes in various line profiles (Walborn et al. 2017). Because HD 269582 appears to be newly entering the LBV phase, studying its variability can be quite instructive. Indeed, a link between light curve structure and outbursts has been proposed for Be stars (Huat et al. 2009; Kurtz et al. 2015); such a link for LBVs may even be testable with an entire year of observations.

The light curve for HD 269582 presented in the third panel of Figure 2 shows coherent $\sim 1\%$ -level variability on timescales of a few days. The periodogram shown in Figure 8 shows a strong peak, detected with prewhitening at $0.20327588 \text{ days}^{-1}$ (corresponding to a 4.919-day period) with small peaks to either side. Though TESS only observed HD 269582 for 5 full cycles of this measured period, the shape of the light curve from cycle to cycle changes noticeably. This can be seen in the dynamic plot in Figure 9, showing the flux as a function of phase from cycle to cycle. The phase of maximum luminosity appears to shift from cycle to cycle, while the amplitude of modulation decreases. Prewhitening reveals the presence of a total of 25 unique frequencies, most of which are small amplitude peaks above $\sim 1 \text{ day}^{-1}$. Among those frequencies, we find no convincing harmonics. Interestingly, two frequencies, $f = 1.6023258$ and $3.1987555 \text{ day}^{-1}$, are found twice each in our search for sums of frequencies.

Similar dominant periods and changes in the light curve shape were observed in WR 110 by Chené et al. (2011). The 30-day light curve presented there appears remarkably similar to the TESS light curve of

Table 3. Summary of the fit results to the periodograms of the six YSGs in our sample, along with their physical properties when available from Neugent et al. (2012). The T_{eff} for HD 270046 is the mean value inferred from the infrared flux in Kunder et al. (2017).

Common Name	Literature Spectral Type	$\log(L/L_{\odot})$	T_{eff}/K	$\alpha_0/10^{-4}$	$\tau/10^{-2}d$	γ	$\alpha_w/10^{-5}$
HD 269953	G0 0 (Keenan & McNeil 1989)	5.437	4920	0.02 ± 0.002	8.79 ± 0.75	3.06 ± 0.28	0.03 ± 0.0001
HD 270046	F8Ia (Ardeberg et al. 1972)	—	6275	0.66 ± 0.306	172.14 ± 63.31	1.76 ± 0.09	0.04 ± 0.0002
HD 270111	G5I (Sanduleak 1970)	—	—	0.13 ± 0.056	84.90 ± 42.58	1.40 ± 0.13	0.04 ± 0.0003
HD 269331	A5Ia (Ardeberg et al. 1972)	5.307	6457	5.56 ± 2.208	100.80 ± 22.10	2.83 ± 0.19	0.10 ± 0.0006
HD 269110	G0I (Ardeberg et al. 1972)	5.251	5624	0.32 ± 0.093	77.23 ± 20.29	1.87 ± 0.13	0.08 ± 0.0003
HD 268687	F6Ia (Ardeberg et al. 1972)	5.169	6081	16.03 ± 2.940	54.06 ± 5.25	2.79 ± 0.07	0.11 ± 0.0005

HD 269582. Chené et al. (2011) attributed the behavior of WR 110 to a CIR in the wind, implying that we are measuring the rotational frequency. It is also possible that this frequency and the surrounding peaks in the periodogram, or the higher frequencies found by prewhitening are nonradial pulsations. Longer monitoring by TESS will enable us to resolve these peaks further, and build a more physical model with well-sampled parameter distributions, and spectroscopic monitoring would allow us to confirm a CIR scenario.

3.2.2. *S Doradus*

S Doradus is the prototypical S Dor variable, with a long history of photometric and spectroscopic observations. van Genderen et al. (1997) detected a ~ 7 year period in S Dor’s light curve, which Abolmasov (2011) argued is more likely to be a timescale associated with the duration of individual flaring events.

The light curve presented in Figure 2 shows strong $\sim 1\%$ variations on sub-day timescales. From the periodogram (Figure 10), it is clear that the variability displayed by S Dor is quite complicated. Prewhitening reveals a total of 41 unique frequencies, the most of any star in the sample. However, we find no harmonics in this list of frequencies. Similar to HD 269582, we find two frequencies (0.66258409 and $1.6460147 \text{ day}^{-1}$) that are each the sum of two different pairs of frequencies. Due to the lack of any single dominant signal, the complexity in the periodogram, and the current theoretical debate on the physical origin of S Dor outbursts, we reserve further modelling until a longer baseline TESS light curve is available, in the hopes of measuring lower frequencies, and resolving the periodogram peaks better.

3.2.3. *LBV Noise Properties*

In addition to our search for coherent variability in the two LBVs, we also analyze the noise properties of their light curves, using Equation 15 to fit the (log of the) Lomb-Scargle periodograms between $1/30 \text{ day}^{-1}$ and the pseudo-Nyquist frequency. The resulting fit pa-

Table 4. Summary of the fit results to the periodograms of the two LBVs in our sample.

Common Name	$\alpha_0/10^{-4}$	$\tau/10^{-2}d$	γ	$\alpha_w/10^{-5}$
HD 269582	6.33 ± 0.74	11.12 ± 0.76	2.96 ± 0.08	0.17 ± 0.0011
S Dor	41.23 ± 7.10	50.55 ± 4.68	2.29 ± 0.03	0.05 ± 0.000

rameters are presented in Table 4, and the fits themselves are shown in Figure 11.

The two LBVs have fairly distinct fit properties, as may be expected given their different temperatures, and the recent evolution of HD 269582 into an LBV state. The noise in the S Dor light curve has a higher α_0 , which may be expected given that the strength of the dominant period in HD 269582. Additionally, we find $\tau \approx 0.5$ day and $\gamma = 2.29$, while HD 269582 has $\tau \approx 0.1$ and $\gamma = 2.96$. In longer-cadence AAVSO data, Abolmasov (2011) fit the power spectra with a pure power law model, and found slopes closer to 2 for strongly flaring objects, and flatter slopes for LBVs in quiescence. While the TESS data don’t probe the low-frequency regime measured by Abolmasov (2011), they do indicate that, in HD 268582, the slope of the stochastic noise is steeper than expected, while in S Dor, the region of the power spectrum where the power-law behavior dominates extends over a wide range of frequencies. This suggests that the variability on sub-day timescales in LBVs may be generated by a mixture of physical processes.

4. DISCUSSION

From this small sample of stars it is impossible to make many sweeping inferences. However, the broad range of light curve characteristics, unexpected characteristic time scales, and the structured noise properties displayed by almost every star in this sample make it clear that rare, evolved massive stars are prime candidates for study with TESS and subsequent missions.

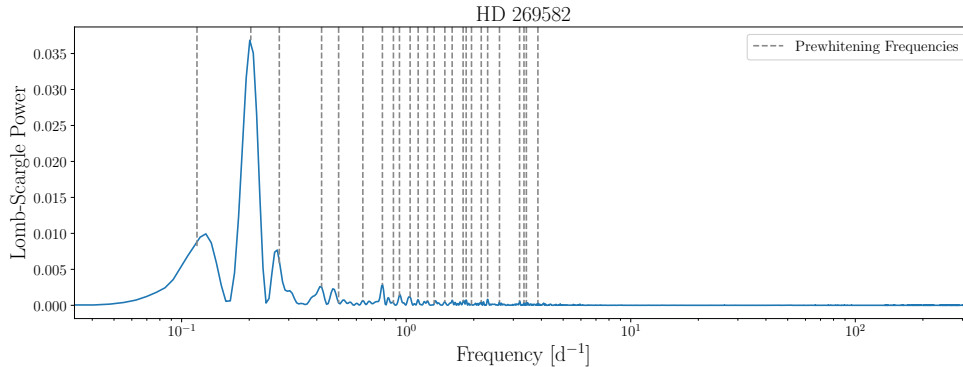


Figure 8. Periodogram for HD 269582, showing a clear peak corresponding to a period of 4.919 days. All frequencies found via prewhitening are indicated with grey vertical lines.

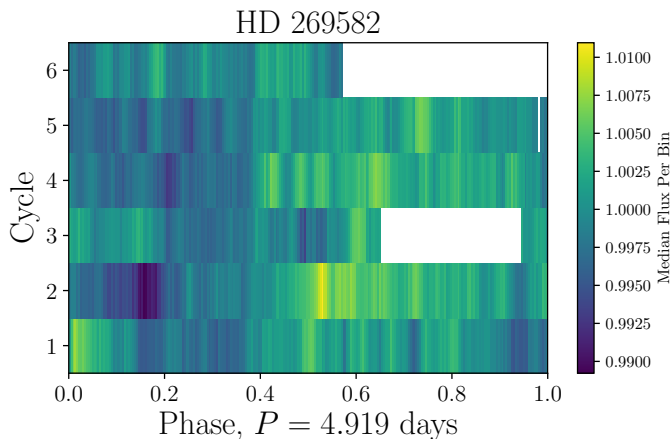


Figure 9. Dynamic plot, phased to a 4.919-day period for HD 269582, showing the variability from cycle to cycle.

Of the light curves that display clear periodicity, only one (the LBV HD 269582) appears to be on a timescale that could be consistent with a rotational period. Rotation is a deeply important parameter for massive stars which can have drastic effects on their evolution (Ekström et al. 2012). Current samples of measured rotation periods in massive stars are insufficient to statistically measure the distribution of rotation rates, leaving us with spectroscopic measurements (e.g., Huang et al. 2010) which are hindered by the unknown inclination of the star relative to the line of sight. *Kepler* has revolutionized the study of stellar rotation for low-mass (FGKM) stars, increasing the known sample from $\sim 10^3$ to over 30,000. Comparison between physical properties and observed rotation periods for low-mass stars from *Kepler* has yielded new insights about magnetic braking evolution and potentially the age distribution of nearby stars in our Galaxy (e.g. van Saders et al. 2016; Davenport & Covey 2018).

None of the light curves we study display a clear signature of binary interactions. Binary interactions are critical in determining the evolution of many (if not most) massive stars. Galactic O stars have an intrinsic binary fraction of at least $\sim 70\%$ (Sana et al. 2012), while the binary fraction in the lower-metallicity LMC appears to be lower (Sana et al. 2013; Dorn-Wallenstein & Levesque 2018). Many of the physics governing these interactions can be constrained by observing post-main-sequence massive stars in binary systems. Unfortunately, very few such systems are known: the observed Wolf-Rayet binary fraction is $\sim 30\%$ (Neugent & Massey 2014), while the binary fraction of yellow and red supergiants is still unknown (Levesque 2017). It is difficult to reconcile these low numbers with the high binary fraction of main sequence stars. Between the complex circumstellar geometry, and the already-complicated spectra of evolved massive stars, the detection of binary systems via radial velocity measurements is arduous. Photometric diagnostics can be used to find candidate RSG+B systems (Neugent et al. 2018), but for many other configurations, photometric variability may be one of the few detectable signatures of binary effects. These variations may manifest themselves as eclipses in well-aligned systems, ellipsoidal variations in short-period systems, or periodic outbursts in extremely eccentric systems as the system approaches periastron. Detecting these effects with TESS and characterizing binary systems with follow-up observations is a critical first step in understanding late-stage massive binary evolution, and resolving the discrepancy between the statistics of main sequence and evolved massive binaries.

Stars with periodicities inconsistent with rotation or binary interactions possess variability on timescales consistent with pulsations. Pulsational modes can give us deep insight into fundamental stellar properties like mass and radius. However, models of both radial and nonradial pulsations in evolved massive stars have only

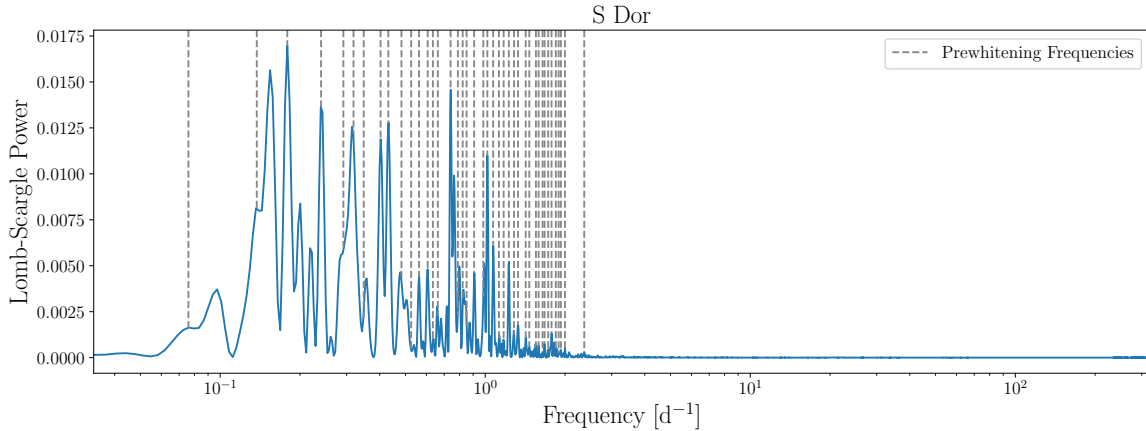


Figure 10. Similar to Figure 8 for S Dor.

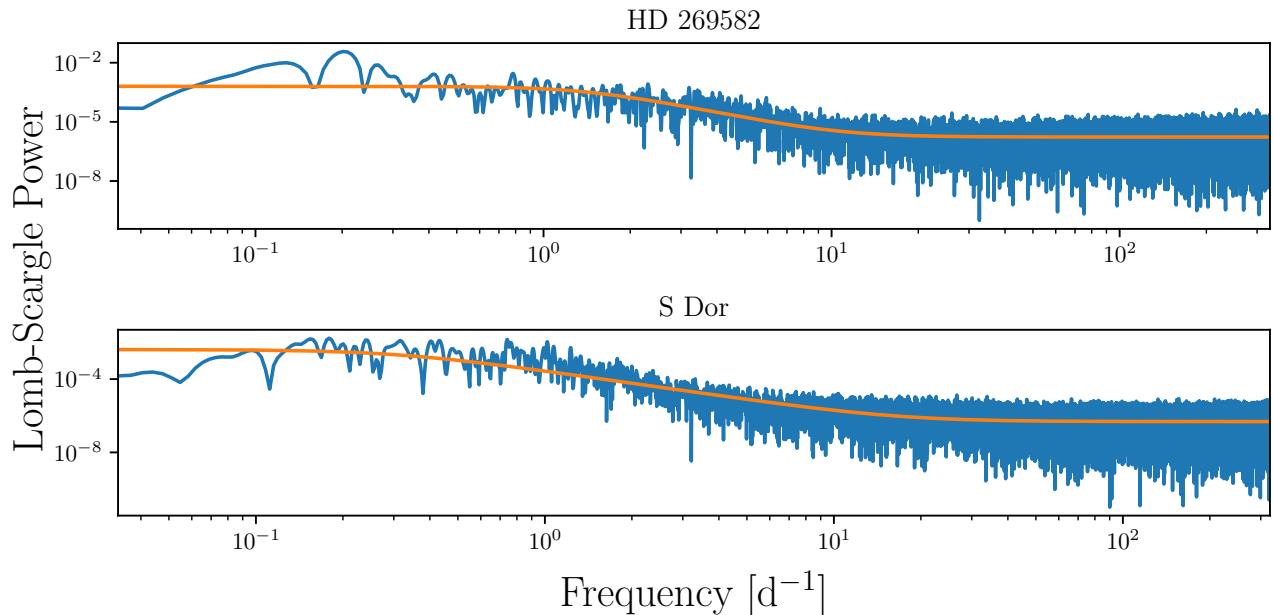


Figure 11. Lomb-Scargle periodograms calculated between $1/30 \text{ day}^{-1}$ and the pseudo-Nyquist frequency for both LBVs. Fits using equation (15) are in orange.

recently been made available (e.g., Jiang et al. 2018). Developing suitable models will allow us to constrain the interior structures of massive stars, and understand energy transport at an unprecedented level. The impact of wave-energy deposition in the last century of a massive star’s life can have important impacts on its pre-supernova evolution (Fuller 2017), and measuring the pulsational properties of the most massive stars will give us valuable constraints on the masses of supernova progenitors.

Finally, red noise is a ubiquitous property in all of the light curves. Whether this noise arises from decoherent

pulsations, surface granulations in the cooler stars, wind instabilities in the hot stars, or some other process entirely, measuring the noise characteristics of a large sample of massive stars will allow us to search for trends as a function of evolutionary stage, which can give us some insight into the physical processes involved. All told, studying evolved massive stars at short timescales can help us answer many unsolved problems in massive star evolution.

5. SUMMARY & CONCLUSION

Our main results are summarized as follows:

- We study eight evolved massive stars. We find distinct periodicity in five stars, including two luminous blue variables, and three yellow supergiants. We are unable to constrain the source of the variability in all cases.
- The light curve of one YSG, HD 269953, displays unique properties not shared by its fellow YSGs. We suggest that it is in a post-RSG evolutionary phase.
- All of the YSGs display red noise in their light curves, that is likely astrophysical in origin.
- The LBV HD 269582 displays 1% variability at ~ 5 day timescales. While the shape of the variability changes, it is possibly due to a rotation period that is imprinting itself into the wind of HD 269582 via a co-rotating interaction region.
- S Doradus exhibits incredible complexity in its periodogram at frequencies below $\sim 1.5 \text{ day}^{-1}$, with a total of 41 unique frequencies found via prewhitening.
- Both LBVs display red noise. The noise in S Dor is stronger (as parametrized by α_0), less steep, and has a longer characteristic timescale τ compared to HD 269582.

We wish to emphasize that evolved massive stars have never been studied before with high cadence space based photometry. As the observed baseline increases for stars in the TESS southern CVZ, the periodogram peaks will grow sharper, and allow us to probe lower frequencies for comparison with previous studies. However, our tentative results presented here highlight the importance of studying massive stars in this domain. It is clear that new models are required to explain the observed variability, which will allow these data to give us an incredibly deep insight into the physics of evolved massive stars.

This work was supported by NSF grant AST 1714285 awarded to E.M.L.

JRAD acknowledges support from the DIRAC Institute in the Department of Astronomy at the University of Washington. The DIRAC Institute is supported through generous gifts from the Charles and Lisa Simonyi Fund for Arts and Sciences, and the Washington Research Foundation

This work made use of the following software:

Software: Astropy v3.0.4 (Astropy Collaboration et al. 2013; The Astropy Collaboration et al. 2018), Matplotlib v2.2.2 (Hunter 2007), makecite v0.4 (Price-Whelan et al. 2018), NumPy v1.15.2 (Van Der Walt et al. 2011), Pandas v0.23.4 (McKinney 2010), Python 3.5.1, SciPy v1.1.0 (Jones et al. 2001–)

APPENDIX

A. FREQUENCIES FOUND VIA PREWHITENING

The following tables contain the list of unique frequencies (separated by $1.5/T$) found by the prewhitening procedure described in §2.2.

REFERENCES

- Aadland, E., Massey, P., Neugent, K. F., & Drout, M. R. 2018, *AJ*, 156, 294, doi: [10.3847/1538-3881/aaeb96](https://doi.org/10.3847/1538-3881/aaeb96)
- Abolmasov, P. 2011, *NewA*, 16, 421, doi: [10.1016/j.newast.2011.03.006](https://doi.org/10.1016/j.newast.2011.03.006)
- Aerts, C., Simón-Díaz, S., Catala, C., et al. 2013, *A&A*, 557, A114, doi: [10.1051/0004-6361/201322097](https://doi.org/10.1051/0004-6361/201322097)
- Aerts, C., Simón-Díaz, S., Bloemen, S., et al. 2017, *A&A*, 602, A32, doi: [10.1051/0004-6361/201730571](https://doi.org/10.1051/0004-6361/201730571)
- Ardeberg, A., Brunet, J. P., Maurice, E., & Prevot, L. 1972, *Astronomy and Astrophysics Supplement Series*, 6, 249
- Arellano Ferro, A. 1985, *MNRAS*, 216, 571, doi: [10.1093/mnras/216.3.571](https://doi.org/10.1093/mnras/216.3.571)
- Astropy Collaboration, Robitaille, T. P., Tollerud, E. J., et al. 2013, *A&A*, 558, A33, doi: [10.1051/0004-6361/201322068](https://doi.org/10.1051/0004-6361/201322068)
- Bailer-Jones, C. A. L., Rybizki, J., Foesneau, M., Mantelet, G., & Andrae, R. 2018, *AJ*, 156, 58, doi: [10.3847/1538-3881/aacb21](https://doi.org/10.3847/1538-3881/aacb21)
- Balona, L. A. 2016, *MNRAS*, 457, 3724, doi: [10.1093/mnras/stw244](https://doi.org/10.1093/mnras/stw244)
- Balona, L. A., Baran, A. S., Daszyńska-Daszkiewicz, J., & De Cat, P. 2015, *MNRAS*, 451, 1445, doi: [10.1093/mnras/stv1017](https://doi.org/10.1093/mnras/stv1017)

Table 5. Unique frequencies, amplitudes, phases, and formal errors for S Dor found via prewhitening. For each frequency, we specify the signal to noise as defined in text, and whether the corresponding signal is significant under the assumption of white noise.

f_j	$\epsilon(f_j)$	A_j	$\epsilon(A_j)$	ϕ_j	$\epsilon(\phi_j)$	SNR	White Noise Significant?
[day ⁻¹]	[day ⁻¹]	[ppt]	[ppt]	[radians]	[radians]		
0.17914669	0.00018699	1.37355329	0.02618908	2.1115	0.0191	1.3475	Y
0.74026962	0.00019105	1.29287459	0.02518611	-2.1163	0.0195	1.2684	Y
0.40287251	0.00019943	1.14940943	0.02337377	3.0257	0.0203	1.1276	Y
0.43090953	0.00019300	1.14783830	0.02258911	2.2956	0.0197	1.1261	Y
1.01866464	0.00020589	1.03719972	0.02177483	-2.7873	0.0210	1.0176	Y
0.31848154	0.00019611	1.05415657	0.02108043	1.5970	0.0200	1.0342	Y
0.29162660	0.00017781	1.12253453	0.02035210	-2.9533	0.0181	1.1013	Y
0.24027468	0.00021217	0.90005164	0.01947179	0.9284	0.0216	0.8830	Y
0.13744498	0.00021613	0.83184153	0.01833204	-1.7119	0.0220	0.8161	Y
1.07115176	0.00022219	0.78722343	0.01783562	1.8799	0.0227	0.7723	Y
0.78858490	0.00022709	0.74934953	0.01735188	-1.3781	0.0232	0.7352	Y
0.90828327	0.00021351	0.77605388	0.01689571	1.7982	0.0218	0.7614	Y
0.48307755	0.00020698	0.77700877	0.01639875	-2.3994	0.0211	0.7623	Y
0.34807760	0.00022384	0.69613397	0.01588865	2.3071	0.0228	0.6830	Y
0.85068961	0.00022519	0.67309428	0.01545560	-1.3659	0.0230	0.6603	Y
0.56272556	0.00022740	0.64883341	0.01504492	-2.4447	0.0232	0.6365	Y
1.22788836	0.00022903	0.62763187	0.01465752	-0.5198	0.0234	0.6157	Y
0.98355185	0.00025223	0.54339970	0.01397567	-2.0356	0.0257	0.5331	Y
0.07590602	0.00025525	0.52566523	0.01368190	-1.4919	0.0260	0.5157	Y
0.60660139	0.00025350	0.51849540	0.01340258	0.4052	0.0258	0.5087	Y
1.33015001	0.00024735	0.47928094	0.01208818	1.8572	0.0252	0.4702	Y
0.52554769	0.00029181	0.39080118	0.01162824	2.6079	0.0298	0.3834	Y
0.63478994	0.00028666	0.38523180	0.01126049	0.3253	0.0292	0.3779	Y
1.12676389	0.00031689	0.33764956	0.01091027	-2.3219	0.0323	0.3313	Y
1.77927887	0.00032095	0.32894596	0.01076545	1.6639	0.0327	0.3227	Y
1.46672799	0.00031496	0.33088598	0.01062659	-2.3816	0.0321	0.3246	Y
1.42147429	0.00035459	0.27557523	0.00996403	-1.6050	0.0362	0.2704	Y
1.28479399	0.00035017	0.27609702	0.00985824	-2.3815	0.0357	0.2709	Y
0.66258409	0.00034800	0.27480157	0.00975139	-0.1970	0.0355	0.2696	Y
1.67496645	0.00035948	0.26019401	0.00953745	2.8436	0.0367	0.2553	Y
1.59025206	0.00034506	0.26826890	0.00943897	-1.8810	0.0352	0.2632	Y
1.72867338	0.00034824	0.26282574	0.00933267	0.6700	0.0355	0.2578	Y
1.89236098	0.00034930	0.25913313	0.00922956	2.8694	0.0356	0.2542	Y
1.17357337	0.00038477	0.22163510	0.00869573	1.7063	0.0392	0.2174	Y
0.82216092	0.00040298	0.20429334	0.00839472	-1.6606	0.0411	0.2004	Y
1.84679016	0.00041217	0.19482554	0.00818812	0.8427	0.0420	0.1911	Y
1.99892588	0.00039723	0.20056820	0.00812403	0.4310	0.0405	0.1968	Y
1.64601470	0.00039939	0.19780379	0.00805566	-0.7468	0.0407	0.1941	Y
1.92956387	0.00041821	0.18733961	0.00798889	-0.3576	0.0426	0.1838	Y
1.55320350	0.00045138	0.16847434	0.00775430	-0.8069	0.0460	0.1653	Y
2.36401361	0.00048031	0.15626593	0.00765330	1.8377	0.0490	0.1533	Y

Table 6. Unique frequencies, amplitudes, phases, and formal errors for HD 269953 found via prewhitening. For each frequency, we specify the signal to noise as defined in text, and whether the corresponding signal is significant under the assumption of white noise.

f_j	$\epsilon(f_j)$	A_j	$\epsilon(A_j)$	ϕ_j	$\epsilon(\phi_j)$	SNR	White Noise Significant?
[day ⁻¹]	[day ⁻¹]	[ppt]	[ppt]	[radians]	[radians]		
1.59360677	0.00033360	0.16933302	0.00576003	-2.4637	0.0340	0.2248	Y
1.17415786	0.00045342	0.12308820	0.00569092	-0.7787	0.0462	0.1634	Y
1.33479243	0.00067704	0.08190471	0.00565440	-1.2113	0.0690	0.1087	Y
0.22397835	0.00077286	0.07154318	0.00563809	2.3700	0.0788	0.0950	Y
2.67017901	0.00084583	0.06522685	0.00562564	0.3010	0.0862	0.0866	Y
0.58964787	0.00123743	0.04450296	0.00561529	-1.1783	0.1262	0.0591	Y
4.00557547	0.00130137	0.04228006	0.00561047	1.8289	0.1327	0.0561	Y
0.79888166	0.00134452	0.04089120	0.00560608	2.3207	0.1371	0.0543	Y
2.35305773	0.00136719	0.04018379	0.00560199	-2.6328	0.1394	0.0533	Y
0.56055207	0.00141498	0.03879914	0.00559803	0.5170	0.1443	0.0515	Y
0.26019548	0.00145392	0.03773483	0.00559432	1.0507	0.1483	0.0501	Y
0.41029670	0.00166929	0.03284581	0.00559081	2.5195	0.1702	0.0436	Y
0.64779043	0.00171080	0.03203336	0.00558813	-3.1395	0.1744	0.0425	Y
0.31217690	0.00180051	0.03042365	0.00558561	0.1242	0.1836	0.0404	N

Table 7. Unique frequencies, amplitudes, phases, and formal errors for HD 269582 found via prewhitening. For each frequency, we specify the signal to noise as defined in text, and whether the corresponding signal is significant under the assumption of white noise.

f_j	$\epsilon(f_j)$	A_j	$\epsilon(A_j)$	ϕ_j	$\epsilon(\phi_j)$	SNR	White Noise Significant?
[day ⁻¹]	[day ⁻¹]	[ppt]	[ppt]	[radians]	[radians]		
0.20327588	0.00026040	2.82300142	0.03653911	1.9457	0.0129	1.4285	Y
0.11705849	0.00038216	1.56893390	0.02980298	-1.8281	0.0190	0.7939	Y
0.27226816	0.00053917	1.02731918	0.02753193	-2.3371	0.0268	0.5199	Y
0.78368008	0.00069788	0.76229473	0.02644290	0.0658	0.0347	0.3857	Y
0.42011270	0.00076838	0.67630930	0.02583021	1.8420	0.0382	0.3422	Y
0.93338470	0.00082913	0.59356109	0.02446216	2.5364	0.0412	0.3004	Y
1.04145053	0.00111576	0.42869614	0.02377533	-1.8655	0.0555	0.2169	Y
1.60232584	0.00110823	0.42783042	0.02356714	-2.4842	0.0551	0.2165	Y
2.30579937	0.00112019	0.41940449	0.02335219	1.7965	0.0557	0.2122	Y
1.84981762	0.00115772	0.39499834	0.02273024	1.7261	0.0575	0.1999	Y
3.19875548	0.00124431	0.36446275	0.02254161	-0.4055	0.0618	0.1844	Y
1.24393495	0.00124528	0.36155380	0.02237916	-2.3360	0.0619	0.1830	Y
0.64113112	0.00136209	0.32818766	0.02221935	-0.2110	0.0677	0.1661	Y
2.60327615	0.00142004	0.31293170	0.02208795	-2.7382	0.0706	0.1584	Y
2.15944146	0.00143368	0.30823824	0.02196565	-1.2146	0.0713	0.1560	Y
1.48653861	0.00144310	0.30457385	0.02184704	3.0061	0.0717	0.1541	Y
0.87749148	0.00150520	0.28886982	0.02161222	-2.1677	0.0748	0.1462	Y
3.42963659	0.00152746	0.28324793	0.02150505	-1.3241	0.0759	0.1433	Y
1.79273050	0.00169152	0.25455605	0.02140248	-0.6712	0.0841	0.1288	Y
1.95391049	0.00168754	0.25415661	0.02131865	-1.6620	0.0839	0.1286	N
1.33240989	0.00234358	0.18158923	0.02115312	-0.4892	0.1165	0.0919	N
1.13080040	0.00161657	0.26272929	0.02111096	-2.4513	0.0804	0.1329	Y
0.50022915	0.00173592	0.24363786	0.02102219	-0.9353	0.0863	0.1233	Y
3.86015782	0.00167586	0.25044910	0.02086229	-1.1760	0.0833	0.1267	Y
3.34708610	0.00170259	0.24554829	0.02078023	-2.5729	0.0846	0.1243	Y

Table 8. Unique frequencies, amplitudes, phases, and formal errors for HD 270046 found via prewhitening. For each frequency, we specify the signal to noise as defined in text, and whether the corresponding signal is significant under the assumption of white noise.

f_j	$\epsilon(f_j)$	A_j	$\epsilon(A_j)$	ϕ_j	$\epsilon(\phi_j)$	SNR	White Noise Significant?
[day ⁻¹]	[day ⁻¹]	[ppt]	[ppt]	[radians]	[radians]		
0.07243476	0.00030333	0.20507787	0.00634302	-0.3777	0.0309	0.2496	Y
0.17088628	0.00053075	0.11542925	0.00624698	1.5664	0.0541	0.1405	Y
0.11054852	0.00062375	0.09772997	0.00621592	2.9262	0.0636	0.1189	Y
0.03864776	0.00059915	0.10138306	0.00619388	-1.7175	0.0611	0.1234	Y
0.23757177	0.00081819	0.07373290	0.00615146	-0.3369	0.0834	0.0897	Y
0.30727002	0.00088671	0.06790027	0.00613926	-2.1785	0.0904	0.0826	Y
0.26646463	0.00108406	0.05544526	0.00612890	-1.8481	0.1105	0.0675	Y
1.03232899	0.00124699	0.04814869	0.00612224	-2.4317	0.1272	0.0586	Y
0.38422638	0.00153431	0.03905225	0.00610975	2.7074	0.1565	0.0475	Y
1.46213112	0.00165260	0.03621682	0.00610298	-1.3304	0.1685	0.0441	Y

Table 9. Unique frequencies, amplitudes, phases, and formal errors for HD 270111 found via prewhitening. For each frequency, we specify the signal to noise as defined in text, and whether the corresponding signal is significant under the assumption of white noise.

f_j	$\epsilon(f_j)$	A_j	$\epsilon(A_j)$	ϕ_j	$\epsilon(\phi_j)$	SNR	White Noise Significant?
[day ⁻¹]	[day ⁻¹]	[ppt]	[ppt]	[radians]	[radians]		
0.13690821	0.00134854	0.13655040	0.00931212	2.5988	0.0682	0.1563	Y
0.20720738	0.00228811	0.08001971	0.00925903	-2.9088	0.1157	0.0916	Y
0.48123388	0.00267880	0.06819859	0.00923862	-2.4779	0.1355	0.0781	Y
0.28689396	0.00253835	0.07186560	0.00922492	-1.0078	0.1284	0.0823	Y
0.41136823	0.00327074	0.05561540	0.00919881	0.6688	0.1654	0.0637	N
1.10220750	0.00358087	0.05074735	0.00918952	2.2761	0.1811	0.0581	N

Table 10. Unique frequencies, amplitudes, phases, and formal errors for HD 269331 found via prewhitening. For each frequency, we specify the signal to noise as defined in text, and whether the corresponding signal is significant under the assumption of white noise.

f_j	$\epsilon(f_j)$	A_j	$\epsilon(A_j)$	ϕ_j	$\epsilon(\phi_j)$	SNR	White Noise Significant?
[day ⁻¹]	[day ⁻¹]	[ppt]	[ppt]	[radians]	[radians]		
0.09042104	0.00050776	0.61699402	0.01557183	-0.4965	0.0252	0.4745	Y
0.17425772	0.00049282	0.60733804	0.01487734	-2.6545	0.0245	0.4670	Y
0.24876181	0.00072428	0.39309944	0.01415176	-0.3416	0.0360	0.3023	Y
0.48741510	0.00153999	0.18011694	0.01378726	0.6008	0.0765	0.1385	Y
0.31028888	0.00155887	0.17711953	0.01372399	-2.5111	0.0775	0.1362	Y
0.72997431	0.00315091	0.08710461	0.01364212	-0.4636	0.1566	0.0670	Y

Table 11. Unique frequencies, amplitudes, phases, and formal errors for HD 269110 found via prewhitening. For each frequency, we specify the signal to noise as defined in text, and whether the corresponding signal is significant under the assumption of white noise.

f_j	$\epsilon(f_j)$	A_j	$\epsilon(A_j)$	ϕ_j	$\epsilon(\phi_j)$	SNR	White Noise Significant?
[day ⁻¹]	[day ⁻¹]	[ppt]	[ppt]	[radians]	[radians]		
0.55347685	0.00054988	0.15765766	0.00883984	-3.0872	0.0561	0.1345	Y
0.11644097	0.00063650	0.13560965	0.00880137	0.0247	0.0649	0.1156	Y
0.15753531	0.00084280	0.10207525	0.00877217	-2.7811	0.0859	0.0871	Y
0.06899622	0.00092764	0.09256332	0.00875550	0.3983	0.0946	0.0789	Y
0.19233848	0.00121647	0.07031901	0.00872248	-2.6869	0.1240	0.0600	Y
0.03827322	0.00123650	0.06911817	0.00871466	-2.0575	0.1261	0.0589	Y
0.40617680	0.00160856	0.05304164	0.00870001	-0.8097	0.1640	0.0452	N

Table 12. Unique frequencies, amplitudes, phases, and formal errors for HD 268687 found via prewhitening. For each frequency, we specify the signal to noise as defined in text, and whether the corresponding signal is significant under the assumption of white noise.

f_j	$\epsilon(f_j)$	A_j	$\epsilon(A_j)$	ϕ_j	$\epsilon(\phi_j)$	SNR	White Noise Significant?
[day ⁻¹]	[day ⁻¹]	[ppt]	[ppt]	[radians]	[radians]		
0.33981559	0.00016013	0.99396295	0.01623009	2.0925	0.0163	0.7147	Y
0.08920241	0.00018662	0.80772984	0.01537070	1.5642	0.0190	0.5808	Y
0.15510687	0.00020617	0.70324644	0.01478409	-1.6240	0.0210	0.5056	Y
0.27854537	0.00024130	0.58182295	0.01431571	-0.7820	0.0246	0.4183	Y
0.42764474	0.00023359	0.58723924	0.01398757	-0.7239	0.0238	0.4222	Y
0.12802564	0.00026270	0.49788111	0.01333659	1.4333	0.0268	0.3580	Y
0.63934778	0.00026317	0.48760456	0.01308489	-3.0826	0.0268	0.3506	Y
0.04723986	0.00032221	0.37892065	0.01244933	2.3780	0.0329	0.2725	Y
0.22510722	0.00031700	0.38006651	0.01228505	-2.1114	0.0323	0.2733	Y
0.53353809	0.00032444	0.36148395	0.01195896	-2.5173	0.0331	0.2599	Y
0.49649588	0.00039730	0.29148694	0.01180883	-2.3401	0.0405	0.2096	Y
0.68791268	0.00041399	0.27292858	0.01152133	-1.9944	0.0422	0.1962	Y
1.34086866	0.00045333	0.24730899	0.01143192	-2.5120	0.0462	0.1778	Y
0.37663919	0.00048990	0.22604532	0.01129199	-2.2111	0.0500	0.1625	Y
0.91512039	0.00049874	0.21952667	0.01116421	2.4091	0.0509	0.1578	Y
1.84286938	0.00049901	0.21823149	0.01110428	-1.1779	0.0509	0.1569	Y
0.73238778	0.00054246	0.19967911	0.01104494	2.9946	0.0553	0.1436	Y
0.80885741	0.00057409	0.18694716	0.01094361	-1.4790	0.0585	0.1344	Y
0.56637230	0.00058752	0.18116978	0.01085355	-0.1779	0.0599	0.1303	Y
0.94887342	0.00059490	0.17821977	0.01081098	0.5464	0.0607	0.1281	Y
2.76492751	0.00062369	0.16936638	0.01077111	0.0375	0.0636	0.1218	Y
0.86314365	0.00069636	0.15073177	0.01070295	-0.4226	0.0710	0.1084	Y
0.77723411	0.00076226	0.13697958	0.01064685	-1.6051	0.0777	0.0985	N
1.20371478	0.00083481	0.12400270	0.01055564	0.6327	0.0851	0.0892	Y
3.68650176	0.00097373	0.10559870	0.01048488	-0.9334	0.0993	0.0759	Y
0.99151843	0.00101754	0.10078308	0.01045694	2.3637	0.1038	0.0725	Y
0.46094861	0.00124317	0.08212864	0.01041091	-1.0581	0.1268	0.0591	Y
1.28252486	0.00126920	0.08030607	0.01039306	2.7736	0.1294	0.0577	N
1.41451720	0.00145098	0.07008822	0.01036985	0.1645	0.1480	0.0504	N
1.58281137	0.00152920	0.06630589	0.01033905	-1.7477	0.1559	0.0477	N
1.63275628	0.00163583	0.06188241	0.01032218	-1.3461	0.1668	0.0445	N
1.07507415	0.00166747	0.06067859	0.01031709	2.8570	0.1700	0.0436	N
4.60899785	0.00171384	0.05900802	0.01031210	-3.1032	0.1748	0.0424	N

Balona, L. A., Pigulski, A., De Cat, P., et al. 2011, MNRAS, 413, 2403,

doi: [10.1111/j.1365-2966.2011.18311.x](https://doi.org/10.1111/j.1365-2966.2011.18311.x)

Baluev, R. V. 2008, MNRAS, 385, 1279,

doi: [10.1111/j.1365-2966.2008.12689.x](https://doi.org/10.1111/j.1365-2966.2008.12689.x)

Blomme, R., Mahy, L., Catala, C., et al. 2011, A&A, 533, A4, doi: [10.1051/0004-6361/201116949](https://doi.org/10.1051/0004-6361/201116949)

Bonanos, A. Z., Massa, D. L., Sewilo, M., et al. 2009, AJ, 138, 1003, doi: [10.1088/0004-6256/138/4/1003](https://doi.org/10.1088/0004-6256/138/4/1003)

Buysschaert, B., Aerts, C., Bloemen, S., et al. 2015, MNRAS, 453, 89, doi: [10.1093/mnras/stv1572](https://doi.org/10.1093/mnras/stv1572)

Chené, A. N., Moffat, A. F. J., Cameron, C., et al. 2011, ApJ, 735, 34, doi: [10.1088/0004-637X/735/1/34](https://doi.org/10.1088/0004-637X/735/1/34)

Chiavassa, A., Pasquato, E., Jorissen, A., et al. 2011, A&A, 528, A120, doi: [10.1051/0004-6361/201015768](https://doi.org/10.1051/0004-6361/201015768)

Choi, J., Dotter, A., Conroy, C., et al. 2016, ApJ, 823, 102, doi: [10.3847/0004-637X/823/2/102](https://doi.org/10.3847/0004-637X/823/2/102)

Conroy, C., Strader, J., van Dokkum, P., et al. 2018, ApJ, 864, 111, doi: [10.3847/1538-4357/aad460](https://doi.org/10.3847/1538-4357/aad460)

Cranmer, S. R., & Owocki, S. P. 1996, ApJ, 462, 469, doi: [10.1086/177166](https://doi.org/10.1086/177166)

Crowther, P. A., & Smith, L. J. 1997, A&A, 320, 500

- Cutri, R. M., Skrutskie, M. F., van Dyk, S., et al. 2003, *VizieR Online Data Catalog*, 2246
- Daszyńska-Daszkiewicz, J., Ostrowski, J., & Pamyatnykh, A. A. 2013, *MNRAS*, 432, 3153, doi: [10.1093/mnras/stt670](https://doi.org/10.1093/mnras/stt670)
- Daszynska-Daszkiewicz, J., Walczak, P., Szewczuk, W., & Pamyatnykh, A. 2018, *ArXiv e-prints*. <https://arxiv.org/abs/1812.00075>
- Davenport, J. R. A., & Covey, K. R. 2018, *ApJ*, 868, 151
- Dorn-Wallenstein, T. Z., & Levesque, E. M. 2018, *ArXiv e-prints*. <https://arxiv.org/abs/1810.01902>
- Dotter, A. 2016, *ApJS*, 222, 8, doi: [10.3847/0067-0049/222/1/8](https://doi.org/10.3847/0067-0049/222/1/8)
- Ekström, S., Georgy, C., Eggenberger, P., et al. 2012, *A&A*, 537, A146, doi: [10.1051/0004-6361/201117751](https://doi.org/10.1051/0004-6361/201117751)
- Fraser, M., Kotak, R., Pastorello, A., et al. 2015, *MNRAS*, 453, 3886, doi: [10.1093/mnras/stv1919](https://doi.org/10.1093/mnras/stv1919)
- Fuller, J. 2017, *MNRAS*, 470, 1642, doi: [10.1093/mnras/stx1314](https://doi.org/10.1093/mnras/stx1314)
- Gaia Collaboration, Brown, A. G. A., Vallenari, A., et al. 2018a, *A&A*, 616, A1, doi: [10.1051/0004-6361/201833051](https://doi.org/10.1051/0004-6361/201833051)
- Gaia Collaboration, Helmi, A., van Leeuwen, F., et al. 2018b, *A&A*, 616, A12, doi: [10.1051/0004-6361/201832698](https://doi.org/10.1051/0004-6361/201832698)
- García-Segura, G., Langer, N., & Mac Low, M.-M. 1996, *A&A*, 316, 133
- Godart, M., Noels, A., Dupret, M.-A., & Lebreton, Y. 2009, *MNRAS*, 396, 1833, doi: [10.1111/j.1365-2966.2009.14903.x](https://doi.org/10.1111/j.1365-2966.2009.14903.x)
- Gordon, K. D., Clayton, G. C., Misselt, K. A., Landolt, A. U., & Wolff, M. J. 2003, *ApJ*, 594, 279, doi: [10.1086/376774](https://doi.org/10.1086/376774)
- Gvaramadze, V. V., Kniazev, A. Y., Castro, N., & Grebel, E. K. 2018, *ArXiv e-prints*. <https://arxiv.org/abs/1812.00007>
- Habets, G. M. H. J., & Heintze, J. R. W. 1981, *A&AS*, 46, 193
- Huang, W., Gies, D. R., & McSwain, M. V. 2010, *ApJ*, 722, 605, doi: [10.1088/0004-637X/722/1/605](https://doi.org/10.1088/0004-637X/722/1/605)
- Huat, A.-L., Hubert, A.-M., Baudin, F., et al. 2009, *A&A*, 506, 95, doi: [10.1051/0004-6361/200911928](https://doi.org/10.1051/0004-6361/200911928)
- Humphreys, R. M., Weis, K., Davidson, K., & Gordon, M. S. 2016, *ApJ*, 825, 64, doi: [10.3847/0004-637X/825/1/64](https://doi.org/10.3847/0004-637X/825/1/64)
- Hunter, J. D. 2007, *Computing In Science & Engineering*, 9, 90
- Jiang, Y.-F., Cantiello, M., Bildsten, L., et al. 2018, *Nature*, 561, 498, doi: [10.1038/s41586-018-0525-0](https://doi.org/10.1038/s41586-018-0525-0)
- Johnston, C., Buyschaert, B., Tkachenko, A., Aerts, C., & Neiner, C. 2017, *MNRAS*, 469, L118, doi: [10.1093/mnrasl/slx060](https://doi.org/10.1093/mnrasl/slx060)
- Jones, E., Oliphant, T., Peterson, P., et al. 2001–, *SciPy: Open source scientific tools for Python*. <http://www.scipy.org/>
- Keenan, P. C., & McNeil, R. C. 1989, *The Astrophysical Journal Supplement Series*, 71, 245, doi: [10.1086/191373](https://doi.org/10.1086/191373)
- Kiss, L. L., Szabó, G. M., & Bedding, T. R. 2006, *MNRAS*, 372, 1721, doi: [10.1111/j.1365-2966.2006.10973.x](https://doi.org/10.1111/j.1365-2966.2006.10973.x)
- Kovács, G. 2000a, *A&A*, 360, L1. <https://arxiv.org/abs/astro-ph/0007271>
- . 2000b, *A&A*, 363, L1. <https://arxiv.org/abs/astro-ph/0011056>
- Krtićka, J., & Feldmeier, A. 2018, *A&A*, 617, A121, doi: [10.1051/0004-6361/201731614](https://doi.org/10.1051/0004-6361/201731614)
- Kunder, A., Kordopatis, G., Steinmetz, M., et al. 2017, *AJ*, 153, 75, doi: [10.3847/1538-3881/153/2/75](https://doi.org/10.3847/1538-3881/153/2/75)
- Kurtz, D. W., Shibahashi, H., Murphy, S. J., Bedding, T. R., & Bowman, D. M. 2015, *MNRAS*, 450, 3015, doi: [10.1093/mnras/stv868](https://doi.org/10.1093/mnras/stv868)
- Levesque, E. M. 2017, *Astrophysics of Red Supergiants* (IOP Publishing Ltd.), doi: [10.1088/978-0-7503-1329-2](https://doi.org/10.1088/978-0-7503-1329-2)
- Lindgren, L., Hernández, J., Bombrun, A., et al. 2018, *A&A*, 616, A2, doi: [10.1051/0004-6361/201832727](https://doi.org/10.1051/0004-6361/201832727)
- Lomb, N. R. 1976, *Ap&SS*, 39, 447, doi: [10.1007/BF00648343](https://doi.org/10.1007/BF00648343)
- Loumos, G. L., & Deeming, T. J. 1978, *Ap&SS*, 56, 285, doi: [10.1007/BF01879560](https://doi.org/10.1007/BF01879560)
- Lovekin, C. C., & Guzik, J. A. 2014, *MNRAS*, 445, 1766, doi: [10.1093/mnras/stu1899](https://doi.org/10.1093/mnras/stu1899)
- Lucy, L. B., & Sweeney, M. A. 1971, *AJ*, 76, 544, doi: [10.1086/111159](https://doi.org/10.1086/111159)
- Malhan, K., Ibata, R. A., & Martin, N. F. 2018, *MNRAS*, 481, 3442, doi: [10.1093/mnras/sty2474](https://doi.org/10.1093/mnras/sty2474)
- Massey, P., Neugent, K. F., & Levesque, E. M. 2017, *Philosophical Transactions of the Royal Society of London Series A*, 375, 20160267, doi: [10.1098/rsta.2016.0267](https://doi.org/10.1098/rsta.2016.0267)
- Massey, P., Olsen, K. A. G., Hodge, P. W., et al. 2007, *AJ*, 133, 2393, doi: [10.1086/513319](https://doi.org/10.1086/513319)
- Mauerhan, J. C., Smith, N., Filippenko, A. V., et al. 2013, *MNRAS*, 430, 1801, doi: [10.1093/mnras/stt009](https://doi.org/10.1093/mnras/stt009)
- McKinney, W. 2010, in *Proceedings of the 9th Python in Science Conference*, ed. S. van der Walt & J. Millman, 51 – 56
- Moffat, A. F. J., St-Louis, N., Carlos-Leblanc, D., et al. 2018, in *3rd BRITE Science Conference*, ed. G. A. Wade, D. Baade, J. A. Guzik, & R. Smolec, Vol. 8, 37–42

- Montgomery, M. H., & Odonoghue, D. 1999, *Delta Scuti Star Newsletter*, 13, 28
- Mullan, D. J. 1984, *ApJ*, 283, 303, doi: [10.1086/162307](https://doi.org/10.1086/162307)
- Neugent, K. F., Levesque, E. M., & Massey, P. 2018, *AJ*, 156, 225, doi: [10.3847/1538-3881/aae4e0](https://doi.org/10.3847/1538-3881/aae4e0)
- Neugent, K. F., & Massey, P. 2014, *ApJ*, 789, 10, doi: [10.1088/0004-637X/789/1/10](https://doi.org/10.1088/0004-637X/789/1/10)
- Neugent, K. F., Massey, P., Skiff, B., & Meynet, G. 2012, *ApJ*, 749, 177, doi: [10.1088/0004-637X/749/2/177](https://doi.org/10.1088/0004-637X/749/2/177)
- Ostrowski, J., & Daszyńska-Daszkiewicz, J. 2015, *MNRAS*, 447, 2378, doi: [10.1093/mnras/stu2605](https://doi.org/10.1093/mnras/stu2605)
- Ostrowski, J., Daszyńska-Daszkiewicz, J., & Cugier, H. 2017, *ApJ*, 835, 290, doi: [10.3847/1538-4357/835/2/290](https://doi.org/10.3847/1538-4357/835/2/290)
- Papaloizou, J., & Pringle, J. E. 1978, *Monthly Notices of the Royal Astronomical Society*, 182, 423, doi: [10.1093/mnras/182.3.423](https://doi.org/10.1093/mnras/182.3.423)
- Paxton, B., Bildsten, L., Dotter, A., et al. 2011, *ApJS*, 192, 3, doi: [10.1088/0067-0049/192/1/3](https://doi.org/10.1088/0067-0049/192/1/3)
- Paxton, B., Cantiello, M., Arras, P., et al. 2013, *ApJS*, 208, 4, doi: [10.1088/0067-0049/208/1/4](https://doi.org/10.1088/0067-0049/208/1/4)
- Paxton, B., Marchant, P., Schwab, J., et al. 2015, *ApJS*, 220, 15, doi: [10.1088/0067-0049/220/1/15](https://doi.org/10.1088/0067-0049/220/1/15)
- Pedersen, M. G., Chowdhury, S., Johnston, C., et al. 2019, *arXiv e-prints*, arXiv:1901.07576. <https://arxiv.org/abs/1901.07576>
- Perdang, J. 2009, in *EAS Publications Series*, Vol. 38, *EAS Publications Series*, ed. M. Goupil, Z. Koláth, N. Nardetto, & P. Kervella, 43–62
- Press, W. H., Teukolsky, S. A., Vetterling, W. T., & Flannery, B. P. 1992, *Numerical recipes in FORTRAN. The art of scientific computing* (Cambridge University Press)
- Price-Whelan, A., Mechev, A., & jumeroag. 2018, *adrn/makecite: v0.1*, doi: [10.5281/zenodo.1343295](https://doi.org/10.5281/zenodo.1343295). <https://doi.org/10.5281/zenodo.1343295>
- Puls, J., Vink, J. S., & Najarro, F. 2008, *A&A Rv*, 16, 209, doi: [10.1007/s00159-008-0015-8](https://doi.org/10.1007/s00159-008-0015-8)
- Ramiamananantsoa, T., Moffat, A. F. J., Harmon, R., et al. 2018, *MNRAS*, 473, 5532, doi: [10.1093/mnras/stx2671](https://doi.org/10.1093/mnras/stx2671)
- Ricker, G. R., Winn, J. N., Vanderspek, R., et al. 2015, *Journal of Astronomical Telescopes, Instruments, and Systems*, 1, 014003, doi: [10.1117/1.JATIS.1.1.014003](https://doi.org/10.1117/1.JATIS.1.1.014003)
- Saio, H., Kurtz, D. W., Murphy, S. J., Antoci, V. L., & Lee, U. 2018, *MNRAS*, 474, 2774, doi: [10.1093/mnras/stx2962](https://doi.org/10.1093/mnras/stx2962)
- Saio, H., Kuschnig, R., Gautschy, A., et al. 2006, *ApJ*, 650, 1111, doi: [10.1086/507409](https://doi.org/10.1086/507409)
- Sana, H., de Mink, S. E., de Koter, A., et al. 2012, *Science*, 337, 444, doi: [10.1126/science.1223344](https://doi.org/10.1126/science.1223344)
- Sana, H., de Koter, A., de Mink, S. E., et al. 2013, *A&A*, 550, A107, doi: [10.1051/0004-6361/201219621](https://doi.org/10.1051/0004-6361/201219621)
- Sanduleak, N. 1970, *Contributions from the Cerro Tololo Inter-American Observatory*, 89
- Scargle, J. D. 1982, *ApJ*, 263, 835, doi: [10.1086/160554](https://doi.org/10.1086/160554)
- Schwarz, G. 1978, *Ann. Statist.*, 6, 461, doi: [10.1214/aos/1176344136](https://doi.org/10.1214/aos/1176344136)
- Smartt, S. J., Eldridge, J. J., Crockett, R. M., & Maund, J. R. 2009, *MNRAS*, 395, 1409, doi: [10.1111/j.1365-2966.2009.14506.x](https://doi.org/10.1111/j.1365-2966.2009.14506.x)
- Smith, N. 2014, *ARA&A*, 52, 487, doi: [10.1146/annurev-astro-081913-040025](https://doi.org/10.1146/annurev-astro-081913-040025)
- Smith, N., & Tombleson, R. 2015, *MNRAS*, 447, 598, doi: [10.1093/mnras/stu2430](https://doi.org/10.1093/mnras/stu2430)
- Stanishev, V., Kraicheva, Z., Boffin, H. M. J., & Genkov, V. 2002, *A&A*, 394, 625, doi: [10.1051/0004-6361:20021163](https://doi.org/10.1051/0004-6361:20021163)
- Stassun, K. G., Oelkers, R. J., Pepper, J., et al. 2018, *AJ*, 156, 102, doi: [10.3847/1538-3881/aad050](https://doi.org/10.3847/1538-3881/aad050)
- The Astropy Collaboration, Price-Whelan, A. M., Sipőcz, B. M., et al. 2018, *ArXiv e-prints*. <https://arxiv.org/abs/1801.02634>
- Van Der Walt, S., Colbert, S. C., & Varoquaux, G. 2011, *ArXiv e-prints*, arXiv:1102.1523. <https://arxiv.org/abs/1102.1523>
- van Genderen, A. M., Sterken, C., & de Groot, M. 1997, *A&A*, 318, 81
- van Saders, J. L., Ceillier, T., Metcalfe, T. S., et al. 2016, *Nature*, 529, 181
- Vaughan, S. 2005, *A&A*, 431, 391, doi: [10.1051/0004-6361:20041453](https://doi.org/10.1051/0004-6361:20041453)
- Walborn, N. R., Gamen, R. C., Morrell, N. I., et al. 2017, *AJ*, 154, 15, doi: [10.3847/1538-3881/aa6195](https://doi.org/10.3847/1538-3881/aa6195)
- Waters, L. B. F. M. 2010, in *Astronomical Society of the Pacific Conference Series*, Vol. 425, *Hot and Cool: Bridging Gaps in Massive Star Evolution*, ed. C. Leitherer, P. D. Bennett, P. W. Morris, & J. T. Van Loon, 267
- Wood, P. R., Bessell, M. S., & Fox, M. W. 1983, *ApJ*, 272, 99, doi: [10.1086/161265](https://doi.org/10.1086/161265)
- Yoon, S.-C., & Cantiello, M. 2010, *ApJL*, 717, L62, doi: [10.1088/2041-8205/717/1/L62](https://doi.org/10.1088/2041-8205/717/1/L62)